

Towards the Detection of Diffusion Model Deepfakes

Jonas Ricker¹ ^a, Simon Damm¹ ^b, Thorsten Holz² ^c and Asja Fischer¹ ^d

¹Ruhr University Bochum, Bochum, Germany

²CISPA Helmholtz Center for Information Security, Saarbrücken, Germany
{jonas.ricker, simon.damm, asja.fischer}@rub.de, holz@cispa.de

Keywords: Deepfake Detection, Diffusion Models, Generative Adversarial Networks, Frequency Analysis.

Abstract: In the course of the past few years, diffusion models (DMs) have reached an unprecedented level of visual quality. However, relatively little attention has been paid to the detection of DM-generated images, which is critical to prevent adverse impacts on our society. In contrast, generative adversarial networks (GANs), have been extensively studied from a forensic perspective. In this work, we therefore take the natural next step to evaluate whether previous methods can be used to detect images generated by DMs. Our experiments yield two key findings: (1) state-of-the-art GAN detectors are unable to reliably distinguish real from DM-generated images, but (2) re-training them on DM-generated images allows for almost perfect detection, which remarkably even generalizes to GANs. Together with a feature space analysis, our results lead to the hypothesis that DMs produce fewer detectable artifacts and are thus more difficult to detect compared to GANs. One possible reason for this is the absence of grid-like frequency artifacts in DM-generated images, which are a known weakness of GANs. However, we make the interesting observation that diffusion models tend to underestimate high frequencies, which we attribute to the learning objective.

1 INTRODUCTION

In the recent past, diffusion models (DMs) have shown a lot of promise as a method for synthesizing images. Such models provide better (or at least similar) performance compared to generative adversarial networks (GANs) and enable powerful text-to-image models such as DALL-E 2 (Ramesh et al., 2022), Imagen (Saharia et al., 2022), and Stable Diffusion (Rombach et al., 2022). Advances in image synthesis have resulted in very high-quality images being generated, and humans can hardly tell if a given picture is an actual or artificially generated image (so-called *deepfake*) (Nightingale and Farid, 2022). This progress has many implications in practice and poses a danger to our digital society: Deepfakes can be used for disinformation campaigns, as such images appear particularly credible due to their sensory comprehensibility. Disinformation aims to discredit opponents in public perception, to create sentiment for or against

certain social groups, and thus influence public opinion. In effect, deepfakes lead to an erosion of trust in institutions or individuals, support conspiracy theories, and promote a fundamental political camp formation. DM-based text-to-image models entail particular risks, since an adversary can specifically create images supporting their narrative, with very little technical knowledge required. A recent example of public deception featuring DM-generated images—although without malicious intent—is the depiction of Pope Francis in a puffer jacket (Huang, 2023). Despite the growing concern about deepfakes and the continuous improvement of DMs, there is only a limited amount of research on their detection.

In this paper, we conduct an extensive experimental study on the detectability of images generated by DMs. Since previous work on the detection of GAN-generated images (e.g., (Wang et al., 2020; Gragnaniello et al., 2021; Mandelli et al., 2022)) resulted in effective detection methods, we raise the question whether these can be applied to DM-generated images. Our analysis on five state-of-the-art GANs and five DMs demonstrates that existing detection methods suffer from severe performance degradation when applied to DM-generated images, with the AUROC dropping by 15.2% on average compared to GANs. However, we show that by re-training, the detection

^a  <https://orcid.org/0000-0002-7186-3634>

^b  <https://orcid.org/0000-0002-4584-1765>

^c  <https://orcid.org/0000-0002-2783-1264>

^d  <https://orcid.org/0000-0002-1916-7033>

This is the extended version of the paper that was accepted at VISAPP 2024.

accuracy can be drastically improved, proving that images generated by DMs *can* be detected. Remarkably, a detector trained on DM-generated images is capable of detecting images from GANs, while the opposite direction does not hold. Our analysis in feature space suggests that DM-generated images are harder to detect because they contain fewer generation artifacts, particularly in the frequency domain. However, we observe a previously overlooked mismatch towards higher frequencies. Further analysis suggests that this is caused by the training objective of DMs, which favors perceptual image quality instead of accurate reproduction of high-frequency details. We believe that our results provide the foundation for further research on the effective detection of deepfakes generated by DMs. Our code and data are available at <https://github.com/jonasricker/diffusion-model-deepfake-detection>.

2 RELATED WORK

Fake Image Detection. In the wake of the emergence of powerful image synthesis methods, the forensic analysis of deepfake images received increased attention, leading to a variety of detection methods (Verdoliva, 2020). Existing approaches can be broadly categorized into two groups. Methods in the first group exploit either semantic inconsistencies like irregular eye reflections (Hu et al., 2021) or known generation artifacts in the spatial (Nataraj et al., 2019; McCloskey and Albright, 2019) or frequency domain (Frank et al., 2020). The second group uses neural networks to learn a feature representation in which real images can be distinguished from generated ones. Wang et al. demonstrate that training a standard convolutional neural network (CNN) on real and fake images from a single GAN yields a classifier capable of detecting images generated by a variety of unknown GANs (Wang et al., 2020). Given the rapid evolution of generative models, developing detectors which generalize to new generators is crucial and therefore a major field of research (Xuan et al., 2019; Chai et al., 2020; Wang et al., 2020; Cozzolino et al., 2021; Gragnaniello et al., 2021; Girish et al., 2021; Mandelli et al., 2022; Jeong et al., 2022).

Since DMs have been proposed only recently, few works analyze their forensic properties. Farid performs an initial exploration of lighting (Farid, 2022a) and perspective (Farid, 2022b) inconsistencies in images generated by DALL-E 2 (Ramesh et al., 2022), showing that DMs often generate physically implausible scenes. A novel approach specifically targeted at

DMs is proposed in (Wang et al., 2023), who observe that DM-generated images can be more accurately reconstructed by a pre-trained DM than real images. The difference between the original and reconstructed image then serves as the input for a binary classifier. Another work (Sha et al., 2023) focuses on text-to-image models like Stable Diffusion (Rombach et al., 2022). They find that incorporating the prompt with which an image was generated (or a generated caption if the real prompt is not available) into the detector improves classification. In a work related to ours (Corvi et al., 2023b), it is shown that GAN detectors perform poorly on DM-generated images. Therefore, a pressing challenge is to develop *universal* detection methods that are effective against different kinds of generative models, mainly GANs and DMs. Ojha et al. make a first step in this direction (Ojha et al., 2023). Instead of training a classifier directly on real and fake images, which according to their hypothesis leads to poor generalization since the detector focuses on e.g., GAN-specific artifacts, they propose to use a pre-trained vision transformer (CLIP-ViT (Dosovitskiy et al., 2021; Radford et al., 2021)), extended with a final classification layer.

Frequency Artifacts in Generated Images. Zhang et al. were the first to demonstrate that the spectrum of GAN-generated images contains visible artifacts in the form of a periodic, grid-like pattern due to transposed convolution operations (Zhang et al., 2019). These findings were later reproduced (Wang et al., 2020) and extended to the discrete cosine transform (DCT) (Frank et al., 2020). Another characteristic was discovered in (Durall et al., 2020), who showed that GANs are unable to correctly reproduce the spectral distribution of the training data. In particular, generated images contain increased magnitudes at high frequencies. While several works attribute these spectral discrepancies to transposed convolutions (Zhang et al., 2019; Durall et al., 2020) or, more general, up-sampling operations (Frank et al., 2020; Chandrasegaran et al., 2021), no consensus on their origin has yet been reached. Some works explain them by the spectral bias of convolution layers due to linear dependencies (Dzanic et al., 2020; Khayatkhoei and Elgammal, 2022), while others suggest the discriminator is not able to provide an accurate training signal (Chen et al., 2021; Schwarz et al., 2021).

In contrast, whether images generated by DMs exhibit grid-like frequency patterns appears to strongly depend on the specific model (Sha et al., 2023; Corvi et al., 2023a; Ojha et al., 2023). Another interesting observation is made by Rissanen et al. who analyze the generative process of diffusion models in the frequency domain (Rissanen et al., 2023). They

state that diffusion models have an inductive bias according to which, during the reverse process, higher frequencies are added to existing lower frequencies. Other works (Kingma et al., 2021; Song et al., 2022b) experiment with adding Fourier features to improve learning of high-frequency content, the former reporting it leads to much better likelihoods.

3 BACKGROUND ON DMs

DMs are a class of probabilistic generative models, originally inspired by nonequilibrium thermodynamics (Sohl-Dickstein et al., 2015). The most common formulations build either on DDPM (Ho et al., 2020) or the score-based modeling perspective (Song and Ermon, 2019; Song and Ermon, 2020; Song et al., 2022b). Numerous modifications and improvements have been proposed, leading to higher perceptual quality (Nichol and Dhariwal, 2021; Dhariwal and Nichol, 2021; Choi et al., 2022; Rombach et al., 2022) and increased sampling speed (Song et al., 2022a; Liu et al., 2022; Salimans and Ho, 2022; Xiao et al., 2022). In short, DMs model a data distribution by gradually disturbing a sample from this distribution and then learning to reverse this diffusion process. To be more precise, we briefly review the forward and backward process for the seminal work in (Ho et al., 2020). In the diffusion (or forward) process for DDPMs, a sample \mathbf{x}_0 (an image in most applications) is repeatedly corrupted by Gaussian noise in sequential steps $t = 1, \dots, T$ in dependence of a monotonically increasing noise schedule $\{\beta_t\}_{t=1}^T$:

$$q(\mathbf{x}_t|\mathbf{x}_{t-1}) = \mathcal{N}(\sqrt{1-\beta_t}\mathbf{x}_{t-1}, \beta_t\mathbf{I}) . \quad (1)$$

With $\alpha_t := 1 - \beta_t$ and $\bar{\alpha}_t := \prod_{s=1}^t \alpha_s$, we can directly sample from the forward process at arbitrary times:

$$q(\mathbf{x}_t|\mathbf{x}_0) = \mathcal{N}(\sqrt{\bar{\alpha}_t}\mathbf{x}_0, (1 - \bar{\alpha}_t)\mathbf{I}) . \quad (2)$$

The noise schedule is typically designed to satisfy $q(\mathbf{x}_T|\mathbf{x}_0) \approx \mathcal{N}(\mathbf{0}, \mathbf{I})$. During the denoising (or reverse) process, we aim to iteratively sample from $q(\mathbf{x}_{t-1}|\mathbf{x}_t)$ to ultimately obtain a clean image from $\mathbf{x}_T \sim \mathcal{N}(\mathbf{0}, \mathbf{I})$. However, since $q(\mathbf{x}_{t-1}|\mathbf{x}_t)$ is intractable as it depends on the entire underlying data distribution, it is approximated by a deep neural network. More formally, $q(\mathbf{x}_{t-1}|\mathbf{x}_t)$ is approximated by

$$p_\theta(\mathbf{x}_{t-1}|\mathbf{x}_t) = \mathcal{N}(\mu_\theta(\mathbf{x}_t, t), \Sigma_\theta(\mathbf{x}_t, t)) , \quad (3)$$

where mean μ_θ and covariance Σ_θ are given by the output of the model (or the latter is set to a constant as proposed in (Ho et al., 2020)). Predicting the mean of the denoised sample $\mu_\theta(\mathbf{x}_t, t)$ is conceptually equivalent to predicting the noise that should be removed,

denoted by $\varepsilon_\theta(\mathbf{x}_t, t)$. Predominantly, the latter approach is implemented (e.g., (Ho et al., 2020; Dhariwal and Nichol, 2021)) such that training a DM boils down to minimizing a (weighted) mean squared error (MSE) $\|\varepsilon - \varepsilon_\theta(\mathbf{x}_t, t)\|^2$ between the true and predicted noise. Note that this objective can be interpreted as a weighted ELBO with data augmentation (Kingma and Gao, 2023). For a recent overview on DMs see (Yang et al., 2023).

4 DATASET

To ensure technical correctness, we decide to analyze a set of generative models for which pre-trained checkpoints and/or samples of *the same* dataset, namely LSUN Bedroom (Yu et al., 2016) (256×256), are available. Otherwise, both the detectability of generated samples and their spectral properties might suffer from biases, making them difficult to compare. An overview of the dataset is given in Table 1 and we provide details and example images in Appendix A.1.

All samples are either directly downloaded or generated using code and pre-trained models provided by the original publications. We consider data from ten models in total, five GANs and five DMs. This includes the seminal models ProGAN (Karras et al., 2018) and StyleGAN (Karras et al., 2019), as well as the more recent ProjectedGAN (Sauer et al., 2021). Note that Diff(usion)-StyleGAN2 and Diff(usion)-ProjectedGAN (Wang et al., 2022a) (the current state of the art on LSUN Bedroom) use a forward diffusion process to optimize GAN training, but this does not change the GAN model architecture. From the class of DMs, we consider the original DDPM (Ho et al., 2020), its successor ID-

Table 1: Models evaluated in this work. Fréchet inception distances (FIDs) on LSUN Bedroom are taken from the original publications and from (Dhariwal and Nichol, 2021) in the case of IDDPM. The lower the FID, the higher the image quality.

Model Class	Method	FID
GAN	ProGAN	8.34
	StyleGAN	2.65
	ProjectedGAN	1.52
	Diff-StyleGAN2	3.65
	Diff-ProjectedGAN	1.43
DM	DDPM	6.36
	IDDPM	4.24
	ADM	1.90
	PNDM	5.68
	LDM	2.95

DPM (Nichol and Dhariwal, 2021), and ADM (Dhariwal and Nichol, 2021), the latter outperforming several GANs with an FID (Heusel et al., 2017) of 1.90 on LSUN Bedroom. PNDM (Liu et al., 2022) speeds up the sampling process by a factor of 20 using pseudo numerical methods, which can be applied to existing pre-trained DMs. Lastly, LDM (Rombach et al., 2022) uses an adversarially trained autoencoder that transforms an image from the pixel space to a latent space (and back). Training the DM in this more suitable latent space reduces the computational complexity and therefore enables training on higher resolutions. The success of this approach is underpinned by the groundbreaking results of Stable Diffusion, a powerful and publicly available text-to-image model based on LDM.

5 DETECTION ANALYSIS

In this section we analyze how well state-of-the-art fake image detectors can distinguish DM-generated from real images. At first, we apply pre-trained detectors known to be effective against GANs, followed by a study on the generalization abilities of re-trained detectors. Based on our findings, we conduct an in-depth feature space analysis to gain a better understanding on how fake images are detected.

Detection Methods. We evaluate three state-of-the-art CNN-based detectors: Wang2020 (Wang et al., 2020), Gragnaniello2021 (Gragnaniello et al., 2021), and Mandelli2022 (Mandelli et al., 2022). They are supposed to perform well on images from unseen generative models, but it is unclear whether this holds for DM-generated images as well. In Appendix B.1 we provide descriptions of all three detectors.

Performance Metrics. The performance of the analyzed classifiers is estimated in terms of the widely used area under the receiver operating characteristic curve (AUROC). However, the AUROC is overly optimistic as it captures merely the potential of a classifier, but the optimal threshold is usually unknown (Cozzolino et al., 2021). Thus, we adopt the use of the probability of detection at a fixed false alarm rate (Pd@FAR) as an additional metric, which is given as the true positive rate at a fixed false alarm rate. Intuitively, this corresponds to picking the y-coordinate of the ROC curve given an x-coordinate. This metric is a valid choice for realistic scenarios such as large-scale content filtering on social media, where only a small amount of false positives is tolerable. We consider a fixed false alarm rate of 1 %.

Evaluating Pre-Trained Detectors. At first, we test the performance of the pre-trained detectors based on 20000 samples, equally divided into real and generated images. While Wang2020 and Gragnaniello2021 are trained on images from a single GAN (ProGAN or StyleGAN2), Mandelli2022 is trained on images from a diverse set of generative models. The results in the upper half of Table 2 show that all GAN-generated images can be effectively distinguished from real images, with Gragnaniello2021 yielding the best results. For DM-generated, however, the performance of all detectors significantly drops, on average by 15.2 % AUROC compared to GANs. Although the average AUROC of 91.4 % achieved by the best-performing model Gragnaniello2021 (ProGAN variant) appears promising, we argue that in a realistic setting with 1 % tolerable false positives, detecting only 25.7 % of all fake images is unacceptable.

To verify that our findings are not limited to our dataset, we extend our evaluation to images from DMs trained on other datasets, variations of ADM, and popular text-to-image models. We provide details on these additional datasets in Appendix A.2. The results, given in the lower half of Table 2, support the finding that detectors perform significantly worse on DM-generated images. Images from PNDM and LDM trained on LSUN Church are detected better, which we attribute to a dataset-specific bias. In an extended experiment (see Appendix B.4) we also find that image perturbations, like compression or blurring, have a stronger adverse effect on the detectability of DM-generated images.

Generalization of Re-Trained Detectors. Given the findings presented above, the question arises whether DMs evade detection in principle, or whether the detection performance can be increased by re-training a detector.¹ We select the architecture from Wang2020 since the original training code is available and training is relatively efficient. Furthermore, we choose the configuration Blur+JPEG (0.5) as it yields slightly better scores on average. For each of the ten generators, we train a detector according to the authors’ instructions, using 78000 samples for training and 2000 samples for validation (equally divided into real (LSUN Bedroom) and fake). We also consider three aggregated settings in which we train on all images generated by GANs, DMs, and both, respectively.

We report AUROC and Pd@1%FAR for each detector evaluated on all datasets in Figure 1, based on 20000 held-out test samples (10000 real and 10000 fake per generator). All detectors achieve near-

¹We carry out the same evaluation with fine-tuned detectors (see Appendix B.2), leading to very similar results.

Table 2: Detection performance of pre-trained universal detectors. For Wang2020 and Gragnaniello2021, we consider two different variants, respectively. In the upper half, we report the performance of models trained on LSUN Bedroom, while results on additional datasets are given in the second half. The best score (determined by the highest Pd@1%) for each generator is highlighted in bold. We report average scores in gray.

AUROC / Pd@1%	Wang2020		Gragnaniello2021		Mandelli2022	
	Blur+JPEG (0.5)	Blur+JPEG (0.1)	ProGAN	StyleGAN2		
ProGAN	100.0 / 100.0	100.0 / 100.0	100.0 / 100.0	100.0 / 100.0	91.2 / 27.5	
StyleGAN	98.7 / 81.4	99.0 / 84.4	100.0 / 100.0	100.0 / 100.0	89.6 / 14.7	
ProjectedGAN	94.8 / 49.1	90.9 / 34.5	100.0 / 99.3	99.9 / 97.8	59.4 / 2.4	
Diff-StyleGAN2	99.9 / 97.9	100.0 / 99.3	100.0 / 100.0	100.0 / 100.0	100.0 / 99.9	
Diff-ProjectedGAN	93.8 / 43.3	88.8 / 27.2	99.9 / 99.2	99.8 / 96.6	62.1 / 2.8	
Average	97.4 / 74.3	95.7 / 69.1	100.0 / 99.7	99.9 / 98.9	80.4 / 29.5	
DDPM	85.2 / 14.2	80.8 / 9.3	96.5 / 39.1	95.1 / 30.7	57.4 / 0.6	
IDDPM	81.6 / 10.6	79.9 / 7.8	94.3 / 25.7	92.8 / 21.2	62.9 / 1.3	
ADM	68.3 / 3.4	68.8 / 4.0	77.8 / 5.2	70.6 / 2.5	60.5 / 1.8	
PNDM	79.0 / 9.2	75.5 / 6.3	91.6 / 16.6	91.5 / 22.2	71.6 / 4.0	
LDM	78.7 / 7.4	77.7 / 6.9	96.7 / 42.1	97.0 / 48.9	54.8 / 2.1	
Average	78.6 / 9.0	76.6 / 6.8	91.4 / 25.7	89.4 / 25.1	61.4 / 2.0	
ADM (LSUN Cat)	58.4 / 2.5	58.1 / 3.3	60.2 / 4.2	51.7 / 1.8	55.6 / 1.3	
ADM (LSUN Horse)	55.5 / 1.5	53.4 / 2.2	56.1 / 2.7	50.2 / 1.4	44.2 / 0.5	
ADM (ImageNet)	69.1 / 4.1	71.7 / 4.5	72.1 / 3.5	83.9 / 16.6	60.1 / 0.9	
ADM-G-U (ImageNet)	67.2 / 3.7	62.3 / 1.2	66.8 / 1.6	78.9 / 10.2	60.0 / 1.0	
PNDM (LSUN Church)	76.9 / 10.2	77.6 / 12.0	90.9 / 24.5	99.3 / 85.8	56.4 / 1.9	
LDM (LSUN Church)	86.3 / 19.8	82.2 / 14.2	98.8 / 75.5	99.5 / 90.2	58.9 / 1.3	
LDM (FFHQ)	69.4 / 3.6	71.0 / 3.6	91.1 / 25.4	67.2 / 2.1	63.0 / 0.6	
ADM' (FFHQ)	77.7 / 8.7	81.4 / 8.8	87.7 / 17.8	89.0 / 17.2	69.8 / 2.0	
P2 (FFHQ)	79.5 / 8.9	83.2 / 9.2	89.2 / 11.5	91.1 / 18.9	72.5 / 2.7	
Stable Diffusion v1-1	42.4 / 1.5	51.4 / 2.0	73.2 / 4.0	75.2 / 13.6	76.1 / 4.2	
Stable Diffusion v1-5	43.7 / 1.4	52.6 / 2.1	72.9 / 2.8	79.8 / 18.3	75.3 / 4.1	
Stable Diffusion v2-1	46.1 / 1.4	47.3 / 1.1	62.8 / 1.1	55.1 / 1.1	37.0 / 0.5	
Midjourney v5	52.7 / 3.0	57.1 / 3.0	69.9 / 3.3	67.1 / 3.3	18.3 / 0.3	

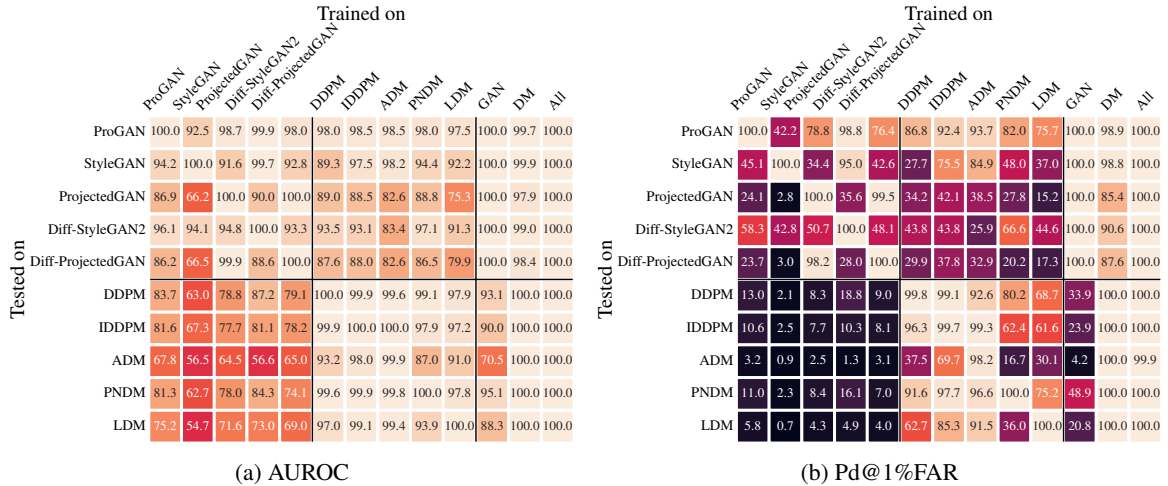


Figure 1: Detection performance for re-trained detectors. The columns *GAN*, *DM*, and *All* correspond to models trained on samples from all GANs, all DMs, and both, respectively.

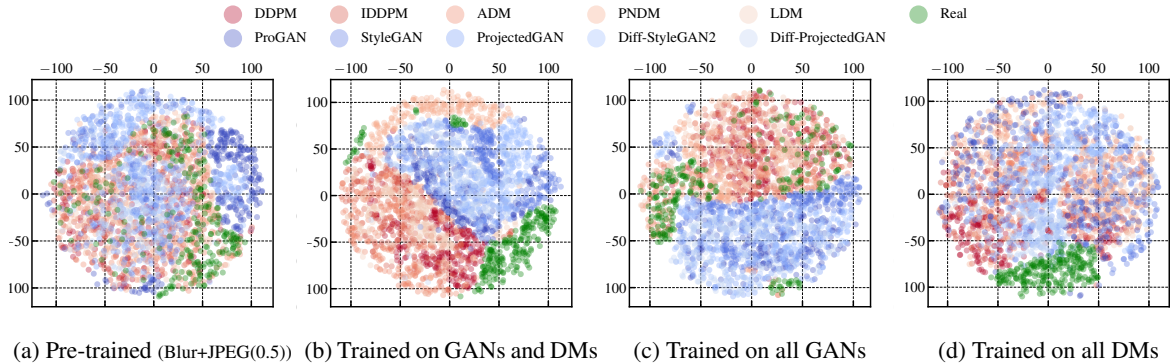


Figure 2: Feature space visualization for the detector Wang2020 via t-SNE of real and generated images in two dimensions. The features correspond to the representation prior to the last fully-connected layer of the given detector.

perfect scores when evaluated on the dataset they were trained on (represented by the values in the diagonal). While this is unsurprising for GANs, it shows that DMs *do* exhibit detectable features that a detector can learn. Regarding generalization, it appears that detectors trained on images from a single DM perform better on images from unseen DMs compared to detectors trained on images from a single GAN. For instance, the detector trained solely on images from ADM achieves a Pd@1%FAR greater than 90% for all other DMs. These findings suggest that images generated by DMs not only contain detectable features, but that these are similar across different architectures and training procedures.

Surprisingly, detectors trained on images from DMs are significantly more successful in detecting GAN-generated images than vice versa. This becomes most apparent when analyzing the detectors that are trained on all GANs and DMs, respectively. While the detector trained on images from all GANs achieves an average Pd@1%FAR of 26.34% on DM-generated images, the detector trained on images from all DMs on average detects 94.26% of all GAN-generated samples.

Analysis of the Learned Feature Spaces. We conduct a more in-depth analysis of the learned feature spaces to better understand this behavior. We utilize t-SNE (van der Maaten and Hinton, 2008) to visualize the extracted features prior to the last fully-connected layer in Figure 2.² For the pre-trained Wang2020 we observe a relatively clear separation between real and GAN-generated images, while there exists a greater overlap between real and DM-generated images (Fig-

²We provide an extended feature space analysis including MMD (Gretton et al., 2012) in Appendix B.3. In Appendix B.5 we additionally show example images considered more or less “fake” based on the detectors’ output scores.

ure 2a). These results match the classification results from Table 2. Looking at the detector which is trained on DM-generated images only (Figure 2d), the feature representations for GAN- and DM-generated images appear to be similar. In contrast, the detectors trained using GAN-generated images or both (Figures 2c and 2b) seem to learn distinct feature representations for GAN- and DM-generated images.

Based on these results, we argue that the hypothesis, according to which a detector trained on one family of generative models cannot generalize to a different family (Ojha et al., 2023), only holds true “in one direction”. Given the feature space visualizations, detectors trained on GAN-generated images appear to focus mostly on GAN-specific artifacts, which may be more prominent and easier to learn. In contrast, a detector trained exclusively on DM-generated images learns a feature representation in which images generated by GANs and DMs are mapped to similar embeddings. As a consequence, this detector *can* generalize to GAN-generated images, since it is not “distracted” by family-specific patterns, but learns to detect artifacts which are present in both GAN- and DM-generated images.

This also implies that DM-generated images contain fewer family-specific artifacts. This becomes apparent when analyzing them in the frequency domain, which we demonstrate in the following section.

6 FREQUENCY ANALYSIS

For detecting GAN-generated images, exploiting artifacts in the frequency domain has proven to be highly effective (Frank et al., 2020). Since DMs contain related building blocks as GANs (especially up-sampling operations in the underlying U-Net (Ronneberger et al., 2015)), it seems reasonable to sus-

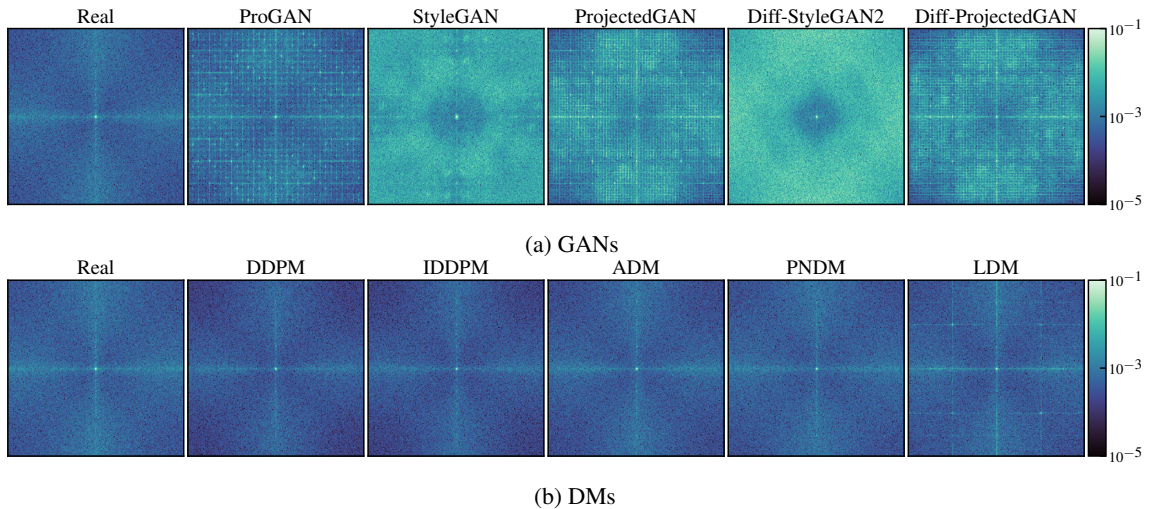


Figure 3: Mean DFT spectrum of real and generated images. To increase visibility, the color bar is limited to $[10^{-5}, 10^{-1}]$, with values lying outside this interval being clipped.

pect that DM-generated exhibit similar artifacts. In this section, we analyze the spectral properties of DM-generated images and compare them to those of GAN-generated images. We investigate potential reasons for the identified frequency characteristics by analyzing the denoising process.

Transforms. We use three frequency transforms that have been applied successfully in both traditional image forensics (Lyu, 2008) and deepfake detection: discrete Fourier transform (DFT), discrete cosine transform (DCT), and the reduced spectrum (Durrall et al., 2020; Dzanic et al., 2020; Schwarz et al., 2021), which is as a 1D representation of the DFT. While DFT and DCT visualize frequency artifacts, the reduced spectrum can be used to identify spectrum discrepancies. The formal definitions of all transforms are provided in Appendix C.1. The DCT-spectra are deferred to Appendix C.2, as well as the frequency analyses of the additional datasets (see Appendix C.7).

Analysis of Frequency Artifacts. Figure 3 depicts the absolute DFT spectrum averaged over 10000 images from each GAN and DM trained on LSUN Bedroom. Before applying the DFT, images are transformed to grayscale and, following previous works (Marra et al., 2019; Wang et al., 2020), high-pass filtered by subtracting a median-filtered version of the image. For all GANs we observe significant artifacts, predominantly in the form of a regular grid, corresponding to previous findings (Zhang et al., 2019; Frank et al., 2020). In contrast, the DFT spectra of images generated by DMs (see Figure 3b), are significantly more similar to the real spectrum with al-

most no visible artifacts. LDM is an exception: while being less pronounced than for GANs, generated images exhibit a clearly visible grid across their spectrum. As mentioned in Section 4, the architecture of LDM differs from the remaining DMs as the final image is generated using an adversarially trained autoencoder, which could explain the discrepancies. This observation supports previous findings which suggest that the discriminator is responsible for spectrum deviations (Chen et al., 2021; Schwarz et al., 2021).

We conclude that “traditional” DMs, which generate images by gradual denoising, do *not* produce the frequency artifacts known from GANs. Regarding our results in Section 5, this could explain why detectors trained on GAN images do not generalize to DMs, while training on DM-generated images leads to better generalization.

In a complementary experiment (see Appendix C.3) inspired by (Frank et al., 2020) we try to answer whether the reduced amount of frequency artifacts makes DM-generated images less detectable in the frequency domain. On the one hand, using a simple logistic regression classifier, DM-generated images can be better classified in the frequency space than in pixel space. On the other hand, the detection accuracy in both frequency and pixel space is significantly lower compared to GAN-generated images, which makes it difficult to draw conclusions. Nevertheless, the fact that a simple classifier performs significantly better on GAN-generated images strengthens the hypothesis that they exhibit stronger artifacts than images generated by DMs.

Analysis of Spectrum Discrepancies. In a second experiment we analyze how well GANs and DMs are

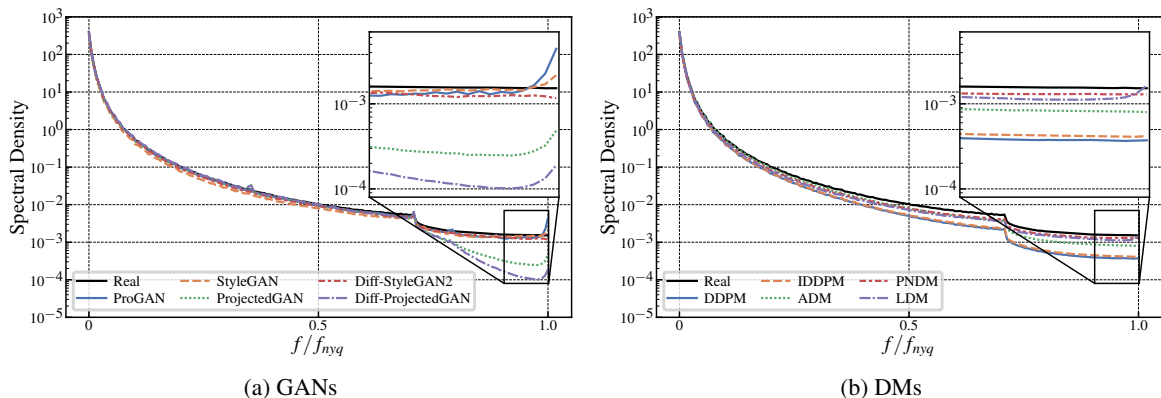


Figure 4: Mean reduced spectrum of real and generated images. The part of the spectrum where GAN-characteristic discrepancies occur is magnified.

able to reproduce the spectral distribution of real images. We visualize the reduced spectra for all generators in Figure 4, again averaged over 10000 images. Except for Diff-StyleGAN2, all GANs contain the previously reported elevated high frequencies. Among the DMs, these can only be observed for LDM. This strengthens the hypothesis that it is this the autoencoder which causes GAN-like frequency characteristics. However, we observe that all DMs have a tendency to underestimate the spectral density towards the higher end of the frequency spectrum. This is particularly noticeable for DDPM, IDDPM, and ADM.

Source of Spectrum Underestimation. Based on these findings, we conduct an additional experiment to identify the source of this spectrum underestimation. Since DMs generate images via gradual denoising, we analyze how the spectrum evolves during this denoising process. For this experiment, we use code and model from ADM (Dhariwal and Nichol, 2021) trained on LSUN Bedroom. We generate samples at different time steps t and compare the reduced spectrum (averaged over 512 images) to that of 50000 real images. The results are shown in Figure 5.

We adopt the figure type from (Schwarz et al., 2021) and depict the relative spectral density error $\tilde{S}_{\text{err}} = \tilde{S}_{\text{fake}}/\tilde{S}_{\text{real}} - 1$, with the colorbar clipped at -1 and 1. At $t = T = 1000$, the image is pure Gaussian noise, which naturally causes strong spectrum deviations. Around $t = 300$, the error starts to decrease, but interestingly it appears that the optimum is not reached at $t = 0$, but at $t \approx 10$. It should be noted that while at this step the frequency spectrum is closest to that of real images, they still contain visible noise (see Fig. 18 in the appendix). During the final denoising steps, \tilde{S}_{err} becomes *negative*, predominantly for higher frequencies, which corresponds to our observations in Figure 4b. In Appendix C.4 we provide

additional results, including the spectral density error between the denoising process and the diffusion process at the corresponding step, which further visualizes this behavior.

We hypothesize that this underestimation towards higher frequencies stems from the learning objective used to train DMs. The full line of thoughts builds on observations from research on denoising autoencoders and is given in Appendix C.5, here we briefly summarize it. Recalling Section 3, DMs are trained to minimize the MSE between the true and predicted noise at different time steps. The weighting of the MSE therefore controls the relative importance of each step. While the semantic content of an image is generated early during the denoising process, high-

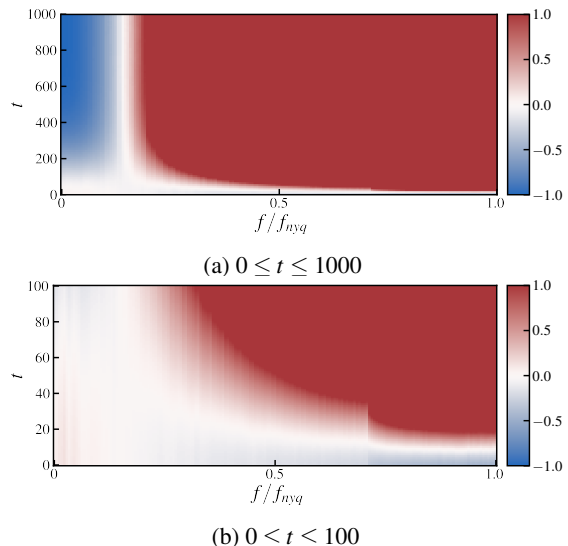


Figure 5: Spectral density error \tilde{S}_{err} throughout the denoising process. The error is computed relative to the spectrum of real images. We display the error for (a) all sampling steps and (b) a close-up of the last 100 steps. The colorbar is clipped at -1 and 1.

frequency details are synthesized near $t = 0$ (Kingma et al., 2021). Theoretically, using the variational lower bound L_{vlb} as the training objective would yield the highest log-likelihood. However, training DMs with L_{vlb} is difficult (Ho et al., 2020; Nichol and Dhariwal, 2021), which is why in practice modified objectives are used. The loss proposed in (Ho et al., 2020), $L_{\text{simple}} = \mathbb{E}_{t, \mathbf{x}_0, \epsilon} [\|\epsilon - \epsilon_\theta(\mathbf{x}_t, t)\|^2]$, for example, considers each denoising step as equally important. Compared to L_{vlb} , the steps near $t = 0$ are significantly down-weighted, trading off a higher perceptual image quality for higher log-likelihood values. The MSE of ADM over t shown in Figure 6 demonstrates that the final denoising steps are the most difficult (which is already plain to see as the signal-to-noise ratio increases for $t \rightarrow 0$, i.e., the to-be-predicted noise makes up ever smaller fractions of \mathbf{x}_t). The hybrid training objective $L_{\text{hybrid}} = L_{\text{simple}} + \lambda L_{\text{vlb}}$ (Nichol and Dhariwal, 2021), used in IDDPM and ADM, incorporates L_{vlb} (with $\lambda = 0.001$) and already improves upon DDPM in modeling the high-frequency details of an image, but still does not match it accurately.

In summary, we conclude that the denoising steps near $t = 0$, which govern the high-frequency content of generated images, are the most difficult to model. By down-weighting the importance of these steps (relatively to the L_{vlb}), DMs achieve remarkable perceptual image quality (or benchmark metrics such as FID), but seem to fall short of accurately matching the high-frequency distribution of real data.

Effect of the Number of Sampling Steps. Lastly, we analyze how the number of sampling steps during the denoising process affects the frequency spectrum. Previous work reported that increasing the number of steps leads to an improved log-likelihood, corresponding to better reproduction of higher frequencies (Nichol and Dhariwal, 2021). Our results in Figure 7 confirm these findings, increasing the number of denoising steps reduces the underestimation. In Appendix C.6 we show that using DDIM (Song et al., 2022a) the spectrum can be reproduced more accurately with fewer steps. We also analyze the de-

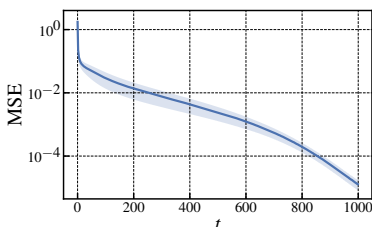


Figure 6: Mean and standard deviation of the MSE for ADM on LSUN Bedroom after training. The denoising steps towards $t = 0$, accounting for high frequencies, have a higher error.

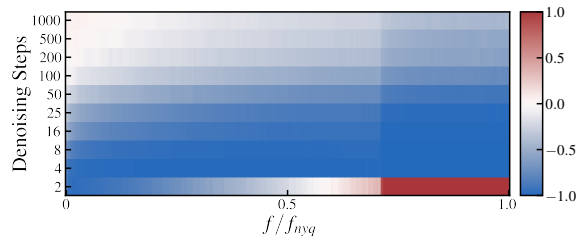


Figure 7: Spectral density error \tilde{S}_{err} for different numbers of denoising steps. The error is computed relatively to the spectrum of real images. The colorbar is clipped at -1 and 1. Note that the y-axis is not scaled linearly.

tectability of images generated with different numbers of denoising steps.

7 CONCLUSION

Deepfakes pose a severe risk for society, and diffusion models have the potential to raise disinformation campaigns to a new level. Despite the urgency of the problem, research about detecting DM-generated images is still in its infancy. In this work, we provide a much-needed step towards the detection of DM deepfakes. Instead of starting from the ground up, we build on previous achievements in the forensic analysis of GANs. We show that, after re-training, current state-of-the-art detection methods can successfully distinguish real from DM-generated images. Further analysis suggests that DMs produce fewer detectable artifacts than GANs, explaining why detectors trained on DM-generated images generalize to GANs, but not vice versa. While artifacts in the frequency domain have been shown to be a characteristic feature of GAN-generated images, we find that DMs predominantly do not have this weakness. However, we observe a systematic underestimation of the spectral density, which we attribute to the loss function of DMs. Whether this mismatch can be exploited for novel detection methods should be part of future research. We hope that our work can foster the forensic analysis of images generated by DMs and spark further research towards the effective detection of deepfakes.

ACKNOWLEDGEMENTS

Funded by the Deutsche Forschungsgemeinschaft (DFG, German Research Foundation) under Germany’s Excellence Strategy - EXC 2092 CASA - 390781972.

REFERENCES

- Chai, L., Bau, D., Lim, S.-N., and Isola, P. (2020). What makes fake images detectable? Understanding properties that generalize. In *European Conference on Computer Vision (ECCV)*.
- Chandrasegaran, K., Tran, N.-T., and Cheung, N.-M. (2021). A closer look at Fourier spectrum discrepancies for CNN-generated images detection. In *IEEE Conference on Computer Vision and Pattern Recognition (CVPR)*.
- Chen, Y., Li, G., Jin, C., Liu, S., and Li, T. (2021). SSD-GAN: Measuring the realness in the spatial and spectral domains. In *AAAI Conference on Artificial Intelligence (AAAI)*.
- Choi, J., Lee, J., Shin, C., Kim, S., Kim, H., and Yoon, S. (2022). Perception prioritized training of diffusion models. In *IEEE Conference on Computer Vision and Pattern Recognition (CVPR)*.
- Corvi, R., Cozzolino, D., Poggi, G., Nagano, K., and Verdoliva, L. (2023a). Intriguing properties of synthetic images: From generative adversarial networks to diffusion models. In *IEEE Conference on Computer Vision and Pattern Recognition (CVPR) Workshops*.
- Corvi, R., Cozzolino, D., Zingarini, G., Poggi, G., Nagano, K., and Verdoliva, L. (2023b). On the detection of synthetic images generated by diffusion models. In *IEEE International Conference on Acoustics, Speech and Signal Processing (ICASSP)*.
- Cozzolino, D., Gagnaniello, D., Poggi, G., and Verdoliva, L. (2021). Towards universal GAN image detection. In *International Conference on Visual Communications and Image Processing (VCIP)*.
- Dhariwal, P. and Nichol, A. (2021). Diffusion models beat GANs on image synthesis. In *Advances in Neural Information Processing Systems (NeurIPS)*.
- Dosovitskiy, A., Beyer, L., Kolesnikov, A., Weissenborn, D., Zhai, X., Unterthiner, T., Dehghani, M., Minderer, M., Heigold, G., Gelly, S., Uszkoreit, J., and Houlsby, N. (2021). An image is worth 16x16 words: Transformers for image recognition at scale. *International Conference on Learning Representations (ICLR)*.
- Durall, R., Keuper, M., and Keuper, J. (2020). Watch your up-convolution: CNN based generative deep neural networks are failing to reproduce spectral distributions. In *IEEE Conference on Computer Vision and Pattern Recognition (CVPR)*.
- Dzanic, T., Shah, K., and Witherden, F. (2020). Fourier spectrum discrepancies in deep network generated images. In *Advances in Neural Information Processing Systems (NeurIPS)*.
- Farid, H. (2022a). Lighting (in)consistency of paint by text. *arXiv preprint*.
- Farid, H. (2022b). Perspective (in)consistency of paint by text. *arXiv preprint*.
- Frank, J., Eisenhofer, T., Schönherr, L., Fischer, A., Kolossa, D., and Holz, T. (2020). Leveraging frequency analysis for deep fake image recognition. In *International Conference on Machine Learning (ICML)*.
- Geras, K. J. and Sutton, C. (2015). Scheduled denoising autoencoders. In *International Conference on Learning Representations (ICLR)*.
- Geras, K. J. and Sutton, C. (2016). Composite denoising autoencoders. In *European Conference on Machine Learning and Knowledge Discovery in Databases (ECML PKDD)*.
- Girish, S., Suri, S., Rambhatla, S. S., and Shrivastava, A. (2021). Towards discovery and attribution of open-world GAN generated images. In *IEEE Conference on Computer Vision and Pattern Recognition (CVPR)*.
- Gagnaniello, D., Cozzolino, D., Marra, F., Poggi, G., and Verdoliva, L. (2021). Are GAN generated images easy to detect? A critical analysis of the state-of-the-art. In *IEEE International Conference on Multimedia and Expo (ICME)*.
- Gretton, A., Borgwardt, K. M., Rasch, M. J., Schölkopf, B., and Smola, A. (2012). A kernel two-sample test. *Journal of Machine Learning Research (JMLR)*, 13(25):723–773.
- He, K., Zhang, X., Ren, S., and Sun, J. (2016). Deep residual learning for image recognition. In *IEEE Conference on Computer Vision and Pattern Recognition (CVPR)*.
- Heusel, M., Ramsauer, H., Unterthiner, T., Nessler, B., and Hochreiter, S. (2017). GANs trained by a two time-scale update rule converge to a local nash equilibrium. In *Advances in Neural Information Processing Systems (NeurIPS)*.
- Ho, J., Jain, A., and Abbeel, P. (2020). Denoising diffusion probabilistic models. In *Advances in Neural Information Processing Systems (NeurIPS)*.
- Hu, S., Li, Y., and Lyu, S. (2021). Exposing GAN-Generated faces using inconsistent corneal specular highlights. In *IEEE International Conference on Acoustics, Speech and Signal Processing (ICASSP)*.
- Huang, K. (2023). Why Pope Francis is the star of A.I.-generated photos. *The New York Times*.
- Hulzebosch, N., Ibrahim, S., and Worring, M. (2020). Detecting CNN-generated facial images in real-world scenarios. In *IEEE Conference on Computer Vision and Pattern Recognition (CVPR) Workshops*.
- Jeong, Y., Kim, D., Ro, Y., Kim, P., and Choi, J. (2022). FingerprintNet: Synthesized fingerprints for generated image detection. In *European Conference on Computer Vision (ECCV)*.
- Karras, T., Aila, T., Laine, S., and Lehtinen, J. (2018). Progressive growing of GANs for improved quality, stability, and variation. In *International Conference on Learning Representations (ICLR)*.
- Karras, T., Laine, S., and Aila, T. (2019). A style-based generator architecture for generative adversarial networks. In *IEEE Conference on Computer Vision and Pattern Recognition (CVPR)*.
- Karras, T., Laine, S., Aittala, M., Hellsten, J., Lehtinen, J., and Aila, T. (2020). Analyzing and improving the image quality of StyleGAN. In *IEEE Conference on Computer Vision and Pattern Recognition (CVPR)*.
- Khayatkhoei, M. and Elgammal, A. (2022). Spatial frequency bias in convolutional generative adversarial

- networks. *AAAI Conference on Artificial Intelligence (AAAI)*.
- Kingma, D., Salimans, T., Poole, B., and Ho, J. (2021). Variational diffusion models. In *Advances in Neural Information Processing Systems (NeurIPS)*.
- Kingma, D. P. and Gao, R. (2023). Understanding diffusion objectives as the ELBO with simple data augmentation. In *Advances in Neural Information Processing Systems (NeurIPS)*.
- Liu, L., Ren, Y., Lin, Z., and Zhao, Z. (2022). Pseudo numerical methods for diffusion models on manifolds. In *International Conference on Learning Representations (ICLR)*.
- Liu, Z., Qi, X., and Torr, P. H. S. (2020). Global texture enhancement for fake face detection in the wild. In *IEEE Conference on Computer Vision and Pattern Recognition (CVPR)*.
- Lyu, S. (2008). *Natural Image Statistics in Digital Image Forensics*. PhD thesis, Dartmouth College.
- Mandelli, S., Bonettini, N., Bestagini, P., and Tubaro, S. (2022). Detecting GAN-generated images by orthogonal training of multiple CNNs. In *IEEE International Conference on Image Processing (ICIP)*.
- Marra, F., Gragnaniello, D., Verdoliva, L., and Poggi, G. (2019). Do GANs leave artificial fingerprints? In *IEEE Conference on Multimedia Information Processing and Retrieval (MIPR)*.
- McCloskey, S. and Albright, M. (2019). Detecting GAN-generated imagery using saturation cues. In *IEEE International Conference on Image Processing (ICIP)*.
- Nataraj, L., Mohammed, T. M., Manjunath, B. S., Chandrasekaran, S., Flenner, A., Bappy, J. H., and Roy-Chowdhury, A. K. (2019). Detecting GAN generated fake images using co-occurrence matrices. *Electronic Imaging*.
- Nichol, A. Q. and Dhariwal, P. (2021). Improved denoising diffusion probabilistic models. In *International Conference on Machine Learning (ICML)*.
- Nightingale, S. J. and Farid, H. (2022). AI-synthesized faces are indistinguishable from real faces and more trustworthy. *Proceedings of the National Academy of Sciences*.
- Ojha, U., Li, Y., and Lee, Y. J. (2023). Towards universal fake image detectors that generalize across generative models. In *IEEE Conference on Computer Vision and Pattern Recognition (CVPR)*.
- Radford, A., Kim, J. W., Hallacy, C., Ramesh, A., Goh, G., Agarwal, S., Sastry, G., Askell, A., Mishkin, P., Clark, J., Krueger, G., and Sutskever, I. (2021). Learning transferable visual models from natural language supervision. In *International Conference on Machine Learning (ICML)*.
- Ramesh, A., Dhariwal, P., Nichol, A., Chu, C., and Chen, M. (2022). Hierarchical text-conditional image generation with CLIP latents. *arXiv preprint*.
- Rissanen, S., Heinonen, M., and Solin, A. (2023). Generative modelling with inverse heat dissipation. In *International Conference on Learning Representations (ICLR)*.
- Rombach, R., Blattmann, A., Lorenz, D., Esser, P., and Ommer, B. (2022). High-resolution image synthesis with latent diffusion models. In *IEEE Conference on Computer Vision and Pattern Recognition (CVPR)*.
- Ronneberger, O., Fischer, P., and Brox, T. (2015). U-Net: Convolutional networks for biomedical image segmentation. In *International Conference on Medical Image Computing and Computer Assisted Intervention*.
- Russakovsky, O., Deng, J., Su, H., Krause, J., Satheesh, S., Ma, S., Huang, Z., Karpathy, A., Khosla, A., Bernstein, M., Berg, A. C., and Fei-Fei, L. (2015). ImageNet large scale visual recognition challenge. *International Journal of Computer Vision (IJCV)*.
- Saharia, C., Chan, W., Saxena, S., Li, L., Whang, J., Denton, E., Ghasemipour, S. K. S., Ayan, B. K., Mahdavi, S. S., Lopes, R. G., Salimans, T., Ho, J., Fleet, D. J., and Norouzi, M. (2022). Photorealistic text-to-image diffusion models with deep language understanding. *arXiv preprint*.
- Salimans, T. and Ho, J. (2022). Progressive distillation for fast sampling of diffusion models. In *International Conference on Learning Representations (ICLR)*.
- Sauer, A., Chitta, K., Müller, J., and Geiger, A. (2021). Projected GANs converge faster. In *Advances in Neural Information Processing Systems (NeurIPS)*.
- Schwarz, K., Liao, Y., and Geiger, A. (2021). On the frequency bias of generative models. In *Advances in Neural Information Processing Systems (NeurIPS)*.
- Sha, Z., Li, Z., Yu, N., and Zhang, Y. (2023). DE-FAKE: Detection and attribution of fake images generated by text-to-image diffusion models. *ACM SIGSAC Conference on Computer and Communications Security (CCS)*.
- Sohl-Dickstein, J., Weiss, E., Maheswaranathan, N., and Ganguli, S. (2015). Deep unsupervised learning using nonequilibrium thermodynamics. In *International Conference on Machine Learning (ICML)*.
- Song, J., Meng, C., and Ermon, S. (2022a). Denoising diffusion implicit models. In *International Conference on Learning Representations (ICLR)*.
- Song, Y. and Ermon, S. (2019). Generative modeling by estimating gradients of the data distribution. In *Advances in Neural Information Processing Systems (NeurIPS)*.
- Song, Y. and Ermon, S. (2020). Improved techniques for training score-based generative models. In *Advances in Neural Information Processing Systems (NeurIPS)*.
- Song, Y., Sohl-Dickstein, J., Kingma, D. P., Kumar, A., Ermon, S., and Poole, B. (2022b). Score-based generative modeling through stochastic differential equations. In *International Conference on Learning Representations (ICLR)*.
- Tan, M. and Le, Q. (2019). EfficientNet: Rethinking model scaling for convolutional neural networks. In *International Conference on Machine Learning (ICML)*.
- van der Maaten, L. and Hinton, G. (2008). Visualizing data using t-SNE. *Journal of Machine Learning Research (JMLR)*.

- Verdoliva, L. (2020). Media forensics and DeepFakes: An overview. *IEEE Journal of Selected Topics in Signal Processing*.
- Vincent, P., Larochelle, H., Lajoie, I., Bengio, Y., and Manzagol, P.-A. (2010). Stacked denoising autoencoders: Learning useful representations in a deep network with a local denoising criterion. *Journal of Machine Learning Research (JMLR)*.
- Wallace, G. K. (1991). The JPEG still picture compression standard. *Communications of the ACM*.
- Wang, S.-Y., Wang, O., Zhang, R., Owens, A., and Efros, A. A. (2020). CNN-generated images are surprisingly easy to spot... for now. In *IEEE Conference on Computer Vision and Pattern Recognition (CVPR)*.
- Wang, Z., Bao, J., Zhou, W., Wang, W., Hu, H., Chen, H., and Li, H. (2023). DIRE for diffusion-generated image detection. *IEEE International Conference on Computer Vision (ICCV)*.
- Wang, Z., Zheng, H., He, P., Chen, W., and Zhou, M. (2022a). Diffusion-GAN: Training GANs with diffusion. *arXiv preprint*.
- Wang, Z. J., Montoya, E., Munechika, D., Yang, H., Hoover, B., and Chau, D. H. (2022b). DiffusionDB: A large-scale prompt gallery dataset for text-to-image generative models. *arXiv preprint*.
- Xiao, Z., Kreis, K., and Vahdat, A. (2022). Tackling the generative learning trilemma with denoising diffusion GANs. In *International Conference on Learning Representations (ICLR)*.
- Xuan, X., Peng, B., Wang, W., and Dong, J. (2019). On the generalization of GAN image forensics. In *Biometric Recognition (CCBR)*.
- Yang, L., Zhang, Z., Song, Y., Hong, S., Xu, R., Zhao, Y., Zhang, W., Cui, B., and Yang, M.-H. (2023). Diffusion models: A comprehensive survey of methods and applications. *ACM Computing Surveys*.
- Yu, F., Seff, A., Zhang, Y., Song, S., Funkhouser, T., and Xiao, J. (2016). LSUN: Construction of a large-scale image dataset using deep learning with humans in the loop. *arXiv preprint*.
- Zhang, X., Karaman, S., and Chang, S.-F. (2019). Detecting and simulating artifacts in GAN fake images. In *IEEE International Workshop on Information Forensics and Security (WIFS)*.

APPENDIX

A DATA COLLECTION

A.1 LSUN Bedroom

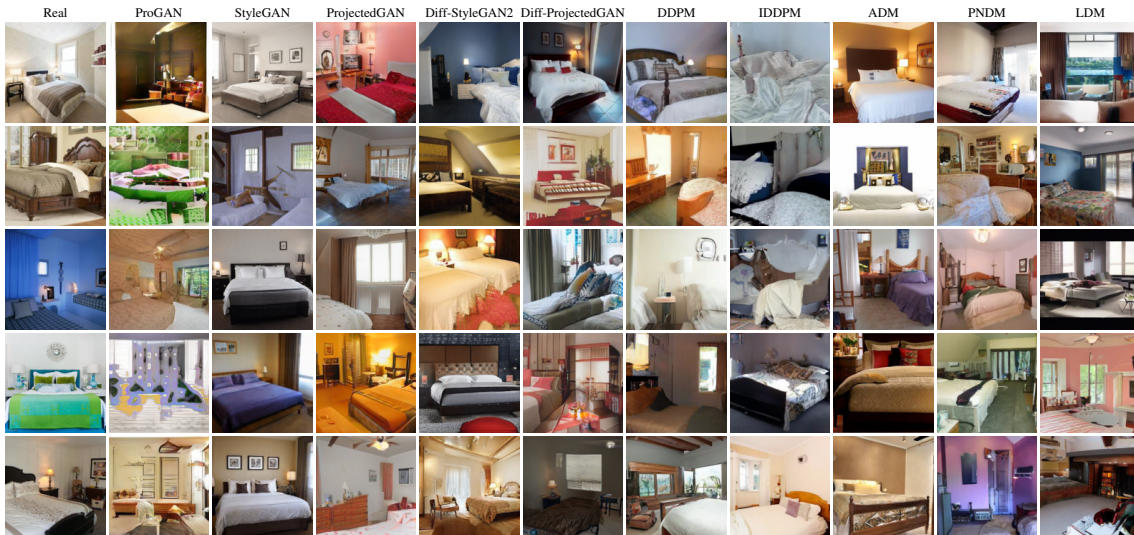


Figure 8: Non-curated example images for real LSUN Bedroom, GAN-generated, and DM-generated images.

LSUN Bedroom (Yu et al., 2016). We download and extract the `lmbd` database files using the official repository³. The images are center-cropped to 256×256 pixels.

ProGAN (Karras et al., 2018). We download the first 10000 samples from the non-curated collection provided by the authors.⁴

StyleGAN (Karras et al., 2019). We download the first 10000 samples generated with $\psi = 0.5$ from the non-curated collection provided by the authors.⁵

ProjectedGAN (Sauer et al., 2021). We sample 10000 images using code and pre-trained models provided by the authors using the default configuration (`--trunc=1.0`).⁶

Diff-StyleGAN2 and Diff-ProjectedGAN (Wang et al., 2022a). We sample 10000 images using code and pre-trained models provided by the authors using the default configuration.⁷

DDPM (Ho et al., 2020), IDDPM (Nichol and Dhariwal, 2021), and ADM (Dhariwal and Nichol, 2021). We download the samples provided by the authors of ADM⁸ and extract the first 10000 samples for each generator. For ADM on LSUN, we select the models trained with dropout.

PNDM (Liu et al., 2022). We sample 10000 images using code and pre-trained model provided by the authors.⁹ We specify `--method F-PNDM` and `--sample_speed 20` for LSUN Bedroom and `--sample_speed 10` for LSUN Church, as these are the settings leading to the lowest FID according to Tables 5 and 6 in the original publication.

³<https://github.com/fyu/lsun>

⁴https://github.com/tkarras/progressive_growing_of_gans

⁵<https://github.com/NVlabs/stylegan>

⁶https://github.com/autonomousvision/projected_gan

⁷<https://github.com/Zhendong-Wang/Diffusion-GAN>

⁸<https://github.com/openai/guided-diffusion>

⁹<https://github.com/luping-liu/PNDM>

LDM (Rombach et al., 2022). We sample 10000 images using code and pre-trained models provided by the authors using settings from the corresponding table in the repository.¹⁰ For LSUN Church there is an inconsistency between the repository and the paper, we choose 200 DDIM steps (`-c 200`) as reported in the paper.

A.2 Additional Datasets

Here we provide details on the additional datasets analyzed in Table 2. Note that ADM-G-U refers to the two-stage up-sampling stack in which images are generated at a resolution of 64×64 and subsequently up-sampled to 256×256 pixels using a second model (Dhariwal and Nichol, 2021). The generated images are obtained according to the instructions given in the previous section.

Due to the relevance of facial images in the context of deepfakes, we also include two DMs not yet considered, P2 and ADM' (Choi et al., 2022), trained on FFHQ (Karras et al., 2019). ADM' is a smaller version of ADM with 93 million instead of more than 500 million parameters.¹¹ P2 is similar to ADM' but features a modified weighting scheme which improves performance by assigning higher weights to diffusion steps where perceptually rich contents are learned (Choi et al., 2022). We download checkpoints for both models from the official repository and sample images according to the authors' instructions.

Real images from LSUN (Yu et al., 2016), ImageNet (Russakovsky et al., 2015), and FFHQ (Karras et al., 2019) are downloaded from their official sources. Images from LSUN Cat/Horse, FFHQ, and ImageNet are resized and cropped to 256×256 pixels by applying the same pre-processing that was used when preparing the training data for the model they are compared against. For all datasets we collect 10000 real and 10000 generated images.

Images from Stable Diffusion¹² are generated using the *diffusers* library¹³ with default settings. For each version, we generate 10000 images using prompts from DiffusionDB (Wang et al., 2022b). Since Midjourney¹⁴ is proprietary, we collect 300 images created using the `"-v 5"` flag from the official Discord server. As real images, we take a subset of 10000 images from LAION-Aesthetics V2¹⁵ with aesthetics scores greater than 6.5. For the detection experiments, we use the entire images, for computing frequency spectra we take center crops of size 256×256 .

¹⁰<https://github.com/CompVis/latent-diffusion>

¹¹<https://github.com/jychoi118/P2-weighting#training-your-models>

¹²<https://stability.ai/blog/stable-diffusion-public-release>

¹³<https://huggingface.co/docs/diffusers/index>

¹⁴<https://www.midjourney.com>

¹⁵<https://laion.ai/blog/laion-aesthetics/>

B SUPPLEMENTAL MATERIAL ON THE DETECTION ANALYSIS

B.1 Descriptions of Detectors

Wang2020 (Wang et al., 2020). In this influential work, the authors demonstrate that a standard deep CNN trained on data from a single generator performs surprisingly well on unseen images. They train a ResNet-50 (He et al., 2016) on 720000 images from 20 LSUN (Yu et al., 2016) categories (not including Bedroom and Church), equally divided into real images and images generated by ProGAN (Karras et al., 2018). The trained binary classifier is able to distinguish real from generated images from a variety of generative models and datasets. The authors further show that extensive data augmentation in the form of random flipping, blurring, and JPEG compression generally improves generalization. Moreover, the authors provide two pre-trained model configurations, Blur+JPEG (0.1) and Blur+JPEG (0.5), where the value in parentheses denotes the probability of blurring and JPEG compression, respectively. They achieve an average precision of 92.6 % and 90.8 %, respectively. The work suggests that CNN-generated images contain common artifacts (or fingerprints) which make them distinguishable from real images.

Gragnaniello2021 (Gragnaniello et al., 2021). Building upon the architecture and dataset from (Wang et al., 2020), the authors of this work experiment with different variations to further improve the detection performance in real-world scenarios. The most promising variant, *no-down*, removes downsampling from the first layer, increasing the average accuracy from 80.71 % to 94.42 %, at the cost of more trainable parameters. They also train a model with the same architecture on images generated by StyleGAN2 (Karras et al., 2020) instead of ProGAN, which further improves the accuracy to 98.48 %.

Mandelli2022 (Mandelli et al., 2022). Unlike the other two methods, this work uses an ensemble of five orthogonal CNNs to detect fake images not seen during training. All CNNs are based on the EfficientNet-B4 model (Tan and Le, 2019) but are trained on different datasets. Dataset orthogonality refers to images having different content, different processing (e.g., JPEG compression), or being generated by different GANs. They argue that by having different datasets, each CNN learns to detect different characteristics of real and generated images, improving the overall performance and generalization ability. For each CNN, a score is computed for ≈ 200 random patches extracted from the image. These scores are combined using a novel patch aggregation strategy which assumes that an image is fake if at least one patch is classified as being fake. Finally, the output score is computed by averaging the individual scores of all five CNNs. It should be noted that, besides several GANs, the training dataset also includes samples generated by a score-based model (Song et al., 2022b).

B.2 Detection Results for Fine-Tuned Classifiers

We repeat the experiment used to generated Figure 1 but fine-tune each classifier instead of re-training it. The results are shown in Figure 9. For most constellations of training and test data, the results are similar compared to those in Figure 1. We suspect that during fine-tuning the existing knowledge is mostly “overwritten”.

		Fine-tuned on												
		ProGAN	StyleGAN	ProjectedGAN	Diff-StyleGAN2	Diff-ProjectedGAN	DDPM	IDDPM	ADM	PNDM	LDM	GAN	DM	All
Tested on	ProGAN	100.0	99.9	100.0	100.0	100.0	99.2	99.3	99.6	99.3	99.8	100.0	99.9	100.0
	StyleGAN	98.5	100.0	98.0	99.9	98.9	95.5	98.2	98.1	96.8	97.8	100.0	99.9	100.0
	ProjectedGAN	93.7	87.8	100.0	94.6	100.0	90.9	91.8	88.2	92.3	86.8	100.0	98.1	100.0
	Diff-StyleGAN2	99.4	99.8	99.3	100.0	99.5	97.6	96.9	84.6	99.1	99.3	100.0	98.9	100.0
	Diff-ProjectedGAN	93.2	86.4	100.0	93.9	100.0	91.0	91.8	89.5	90.3	91.0	100.0	98.6	100.0
	DDPM	82.4	77.5	81.8	88.0	82.6	100.0	99.9	99.7	99.1	98.2	92.4	100.0	100.0
	IDDPM	80.5	77.9	79.7	82.7	81.7	99.8	100.0	99.9	97.9	97.9	89.6	100.0	100.0
	ADM	65.7	61.3	65.2	60.3	67.9	93.3	97.4	99.9	85.9	93.0	69.5	100.0	100.0
	PNDM	77.5	74.3	79.9	83.1	81.8	99.8	99.9	99.8	100.0	99.2	93.3	100.0	100.0
	LDM	76.7	68.1	74.1	77.6	78.0	97.6	99.2	99.5	94.6	100.0	87.9	100.0	100.0

(a) AUROC

		Fine-tuned on												
		ProGAN	StyleGAN	ProjectedGAN	Diff-StyleGAN2	Diff-ProjectedGAN	DDPM	IDDPM	ADM	PNDM	LDM	GAN	DM	All
Tested on	ProGAN	100.0	98.9	99.4	100.0	99.8	95.9	96.5	97.6	94.8	98.0	100.0	99.4	100.0
	StyleGAN	78.5	100.0	70.1	98.8	83.0	60.7	81.8	85.5	67.8	73.6	100.0	98.4	100.0
	ProjectedGAN	40.2	20.0	100.0	55.2	100.0	43.8	51.7	48.8	40.2	37.6	100.0	86.2	100.0
	Diff-StyleGAN2	88.9	96.1	88.9	100.0	92.9	75.2	72.2	39.1	89.5	92.0	100.0	89.7	100.0
	Diff-ProjectedGAN	39.8	17.9	99.5	49.2	100.0	42.0	50.0	47.4	31.0	45.1	100.0	88.9	100.0
	DDPM	10.9	7.1	9.3	19.9	10.0	99.7	99.0	93.5	81.8	72.9	30.3	100.0	100.0
	IDDPM	8.4	7.0	7.4	12.2	9.2	96.1	99.3	98.9	64.5	69.2	22.7	100.0	100.0
	ADM	2.4	1.8	2.4	1.7	3.2	42.0	65.9	97.7	16.5	38.6	4.0	99.7	99.9
	PNDM	6.6	6.3	7.4	14.4	10.9	96.7	98.7	96.6	100.0	89.1	39.4	100.0	100.0
	LDM	5.7	2.9	4.4	7.8	6.6	68.4	86.2	92.7	40.8	100.0	20.6	100.0	100.0

(b) Pd@1%

Figure 9: Detection performance for fine-tuned detectors. The columns *GAN*, *DM*, and *All* correspond to models trained on samples from all GANs, all DMs, and both, respectively.

B.3 Extended Feature Space Analysis

We extend the feature space analysis conducted in Section 5 by estimating the distance between the distributions of real and generated images in feature space using maximum mean discrepancy (MMD, (Gretton et al., 2012)). The 2048-dimensional features are extracted prior to the last fully-connected layer of the detectors Wang2020 and Gragnaniello2021. We employ a Gaussian kernel with σ as the median distance between instances in the combined sample as suggested by (Gretton et al., 2012) and calculate the MMD between the representations of 10000 generated and 10000 real images.

We consider three sets of detection methods, namely pre-trained, fine-tuned and re-trained from scratch. Starting with pre-trained detection methods (top row in Figure 10), we observe that the MMD between representations of DM-generated images and those of real images are considerably lower in comparison to GAN-generated images. With the results from Table 2 in mind, we can conclude that the pre-trained detectors extract features that allow to reliably separate GAN-generated images from real images, while these features are less informative to spot DM-generated images.

When fine-tuning/re-training on generated images from both, DMs and GANs, the MMDs in feature space are roughly on par for both model sets (middle and bottom row in Figure 10). When fine-tuning/training solely on images from one model class we observe an imbalance: Detectors fine-tuned or trained on images from DMs are able to achieve relatively higher MMDs for GAN-generated images than vice versa, supporting our previous findings.

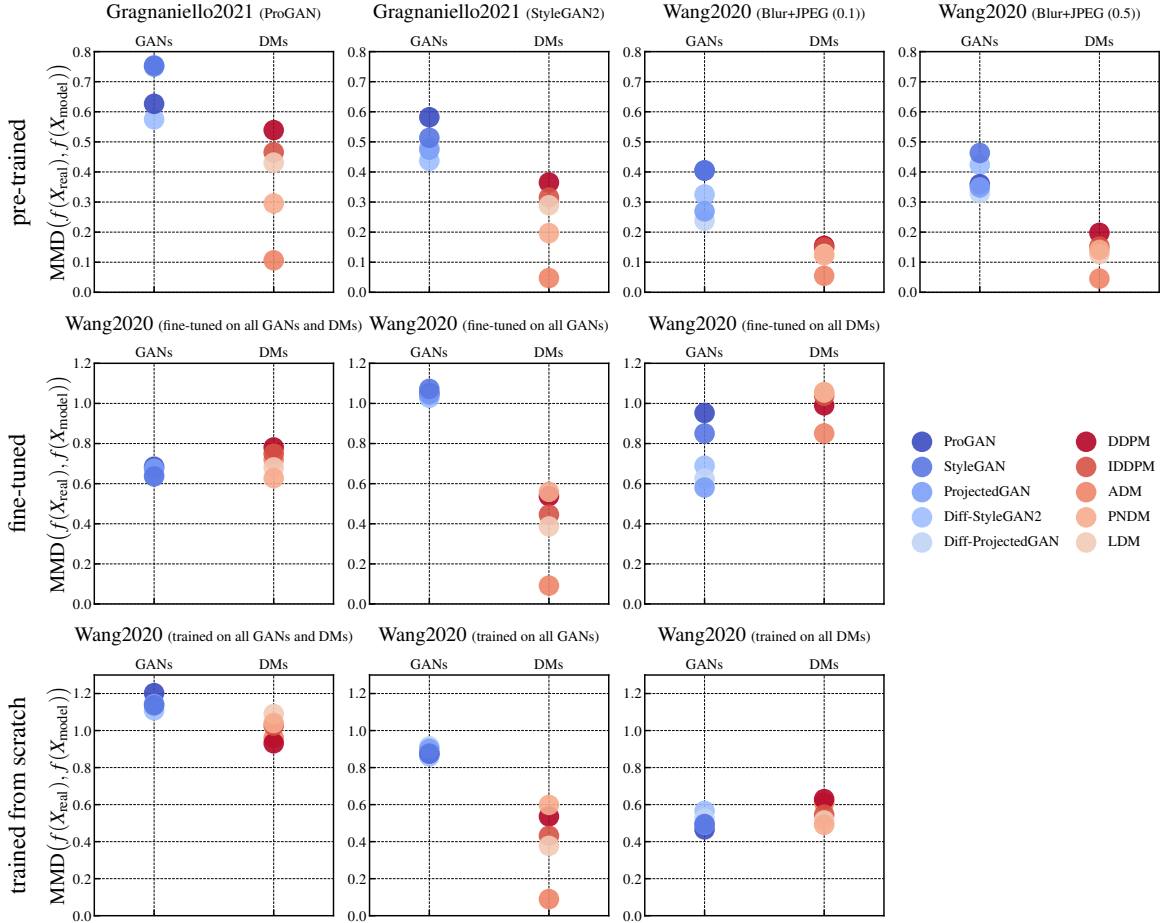


Figure 10: Feature space visualization for different detectors (pre-trained, fine-tuned and trained from scratch) via MMD of real (LSUN Bedroom) and generated images. The features $f(\cdot)$ correspond to the representation prior to the last fully-connected layer of the respective detection method.

For completeness, we provide the t-SNE visualizations (van der Maaten and Hinton, 2008) analogous to Figure 10 in Figure 11. We use the scikit-learn implementation of t-SNE with the default settings for all 110000 images in our dataset (10000 images per GAN/DM and 10000 real images) and visualize 250 images per class.

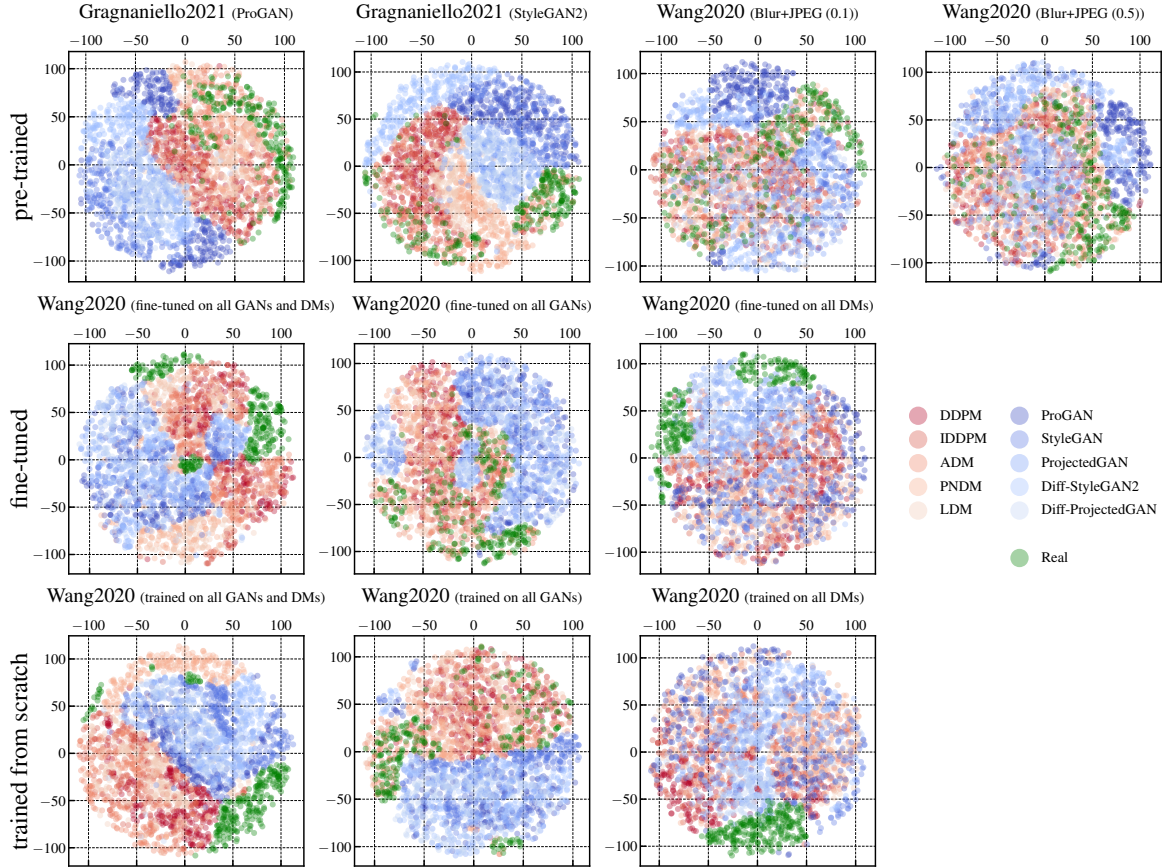


Figure 11: Feature space visualization for different detectors (pre-trained, fine-tuned and trained from scratch) via t-SNE of real (LSUN Bedroom) and generated images in two dimensions. The features correspond to the representation prior to the last fully-connected layer of the respective detection method.

B.4 Effect of Image Perturbations

In most real-world scenarios, like uploading to social media, images are processed, which is why several previous works consider common image perturbations when evaluating detectors (Wang et al., 2020; Hulzebosch et al., 2020; Liu et al., 2020; Frank et al., 2020). We follow the protocol of (Frank et al., 2020) and apply blurring using a Gaussian filter (kernel size sampled from $\{3, 5, 7, 9\}$), cropping with subsequent upsampling (crop factor sampled from $U(5, 20)$), JPEG compression (quality factor sampled from $U(10, 75)$), and Gaussian noising (variance sampled from $U(5, 20)$). Unlike (Frank et al., 2020), we apply each perturbation with a probability of 100 % to study its effect on the detection performance.

Table 3 shows the results for the best-performing detector Gragnaniello2021 trained on ProGAN images. Note that this detection method employs training augmentation using blurring and JPEG compression. We copy the results on “clean” images from Table 2 as a reference. For GAN-generated images, blurring and cropping have only a very small effect on the detection performance, while compression and the addition of noise cause a stronger deterioration (1 % and 3.4 % average AUROC decrease, respectively). Overall, we observe that perturbations (except for cropping) have a stronger effect on DM-generated images compared to GAN-generated images. On average, the AUROC decreases by 12.66 % for blurring, 14.98 % for compression, and 12.18 % for noise. We repeat the experiment using the detector Wang2020 fine-tuned on images from all DMs (see Appendix B.2). As

the results in Table 4 show, the effect of blurring and cropping is now almost negligible. The performance drop caused by JPEG compression is also significantly smaller (2.42 % average AUROC decrease). While fine-tuning improves the results for these three perturbations, the same does not hold for adding Gaussian noise. The latter could be related to the fact that the image generation process of DMs involves noise. However, another potential explanation is that the detector is shown blurred and compressed images during training but not those with added noise.

Table 3: Effect of image perturbations on detection performance. We use the pre-trained detector Gragnaniello2021 trained on ProGAN images and compute metrics from 10000 samples.

AUROC / Pd@1%	Clean	Blur	Crop	JPEG	Noise
ProGAN	100.0 / 100.0	100.0 / 100.0	100.0 / 100.0	100.0 / 98.6	99.2 / 82.5
StyleGAN	100.0 / 100.0	99.7 / 94.3	100.0 / 99.9	99.0 / 79.9	94.3 / 40.9
ProjectedGAN	100.0 / 99.3	99.2 / 87.6	99.9 / 98.0	98.2 / 71.7	96.6 / 52.8
Diff-StyleGAN2	100.0 / 100.0	100.0 / 100.0	100.0 / 100.0	99.7 / 92.7	96.7 / 56.3
Diff-ProjectedGAN	99.9 / 99.2	99.0 / 84.1	99.9 / 97.0	98.1 / 70.6	96.1 / 51.0
DDPM	96.5 / 39.1	78.5 / 8.1	95.5 / 35.2	81.1 / 6.3	85.1 / 11.2
IDDPM	94.3 / 25.7	75.3 / 5.5	93.5 / 24.6	77.5 / 5.0	80.9 / 7.0
ADM	77.8 / 5.2	66.0 / 3.0	78.3 / 5.5	64.1 / 1.6	64.8 / 1.7
PNDM	91.6 / 16.6	86.7 / 14.3	91.1 / 19.7	76.0 / 3.9	81.2 / 9.3
LDM	96.7 / 42.1	87.1 / 17.1	96.8 / 48.9	83.3 / 8.3	82.2 / 8.8

Table 4: Effect of image perturbations on detection performance. We use the detector Wang2020 fine-tuned on all DM-generated images and compute metrics from 10000 samples.

AUROC / Pd@1%	Clean	Blur	Crop	JPEG	Noise
DDPM	100.0 / 100.0	100.0 / 99.9	100.0 / 99.9	98.5 / 80.1	69.8 / 11.3
IDDPM	100.0 / 100.0	100.0 / 100.0	100.0 / 100.0	98.1 / 75.8	70.2 / 11.1
ADM	100.0 / 99.7	99.9 / 99.0	100.0 / 99.5	94.5 / 47.1	70.3 / 10.8
PNDM	100.0 / 100.0	100.0 / 99.8	100.0 / 100.0	98.7 / 84.5	74.8 / 14.6
LDM	100.0 / 100.0	100.0 / 100.0	100.0 / 100.0	98.1 / 77.3	71.9 / 12.9

B.5 Fakeness Rating

We evaluate whether DM-generated images exhibit some visual cues used by the detector to distinguish them from real images. Inspired by (Wang et al., 2020), we rank all images by the model’s predictions (higher value means “more fake”) and show examples from different percentiles. We consider two detectors, the pre-trained detector Gragnaniello2021 trained on ProGAN (Figure 12) and the detector Wang2020 fine-tuned on all DM-generated images (Figure 13). Using Gragnaniello2021, we make the observation that for most DMs, images which the model assigns a high “fakeness” score contain many pixels which are purely white or black. On the other hand, images considered less fake appear to be more colorful. We were able to reproduce this behavior for other datasets in Figure 14. However, this finding does not hold for the ranking provided by the fine-tuned detector. Overall, we agree with (Wang et al., 2020) that there is no strong correlation between the model’s predictions and visual quality.

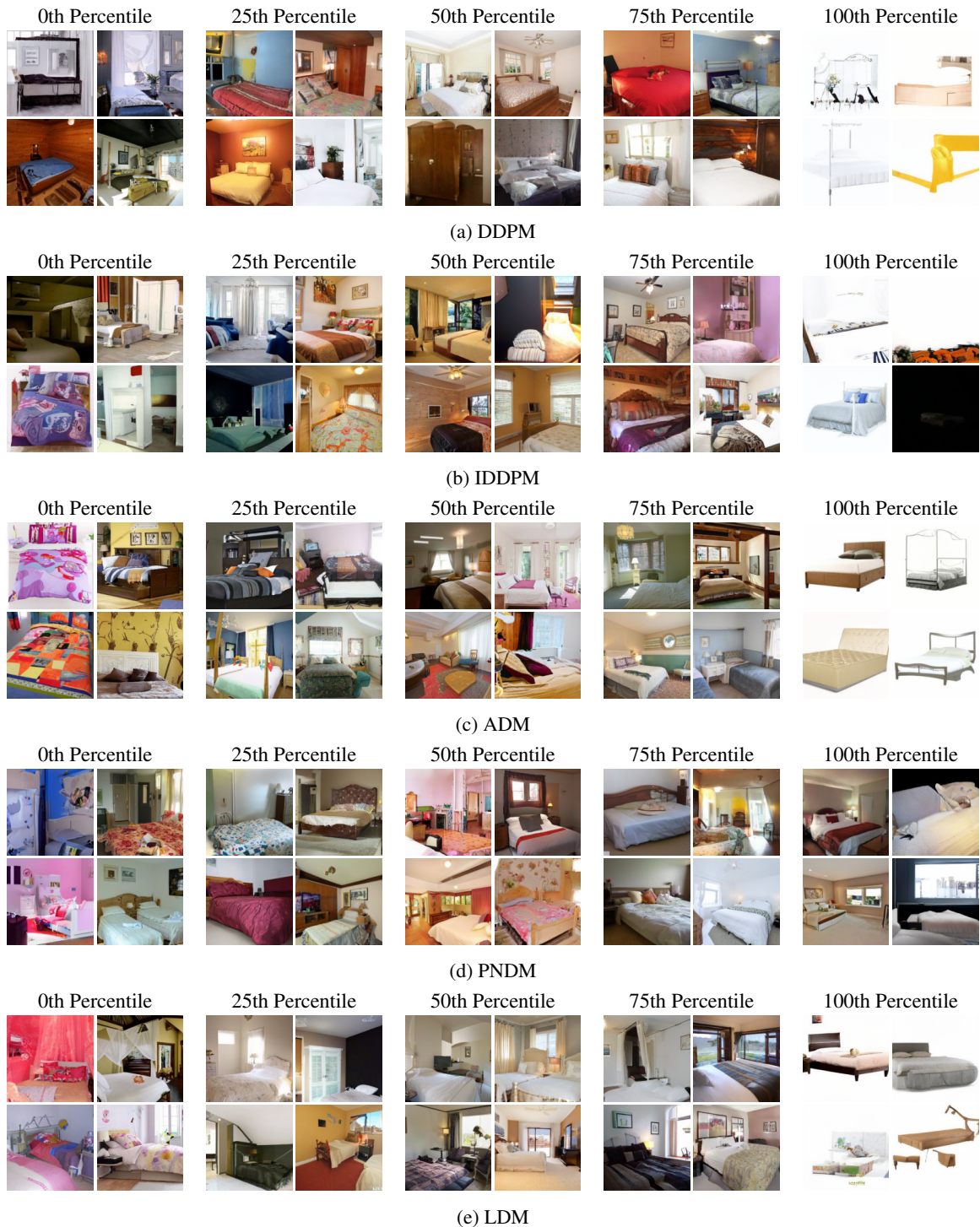


Figure 12: “Fakeness” rating based of DM-generated images (LSUN Bedroom) on predictions from detector Grgananiello2021 trained on ProGAN images. Images are ranked by the model’s output, i.e., images in the 100th percentile are considered most fake.

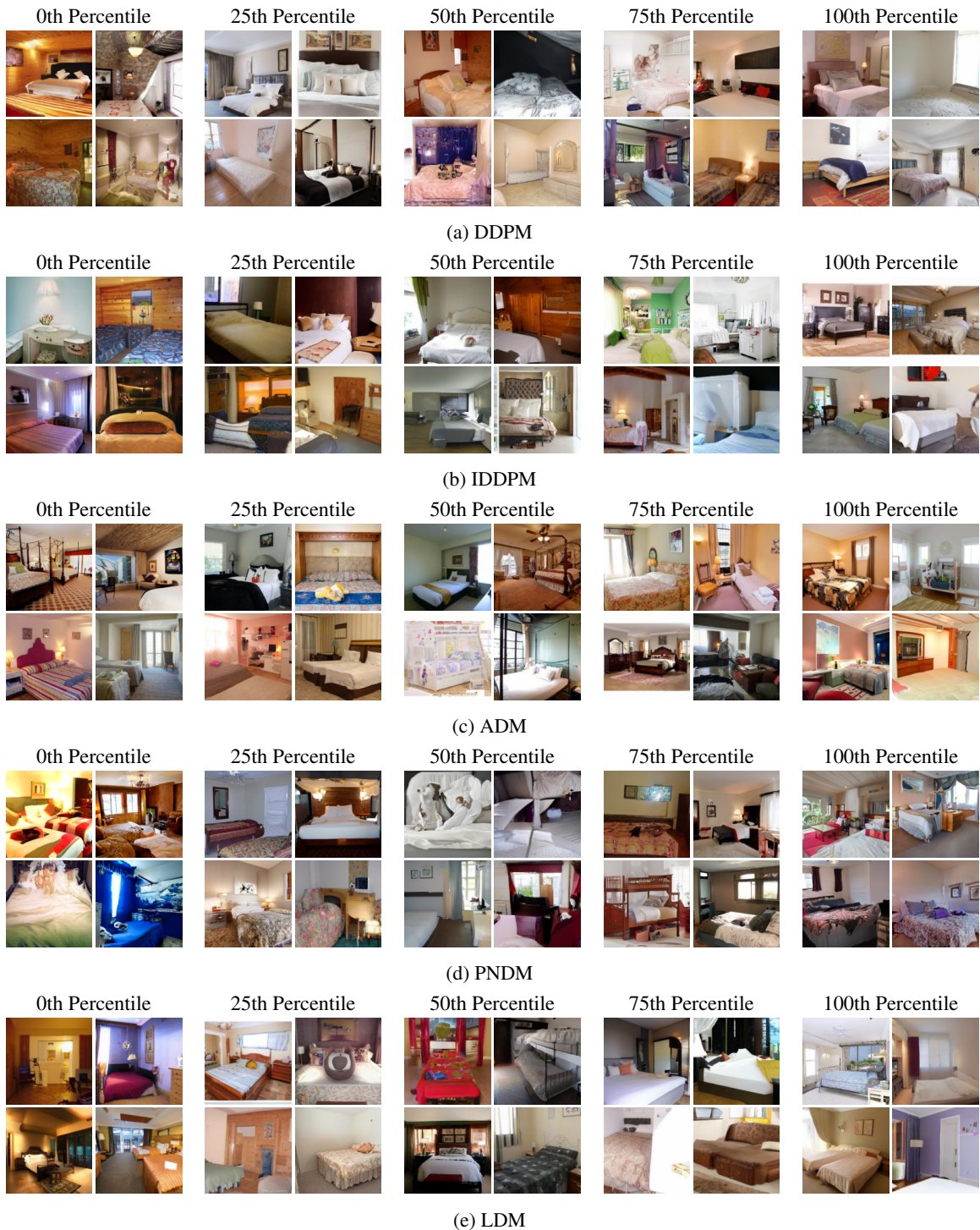
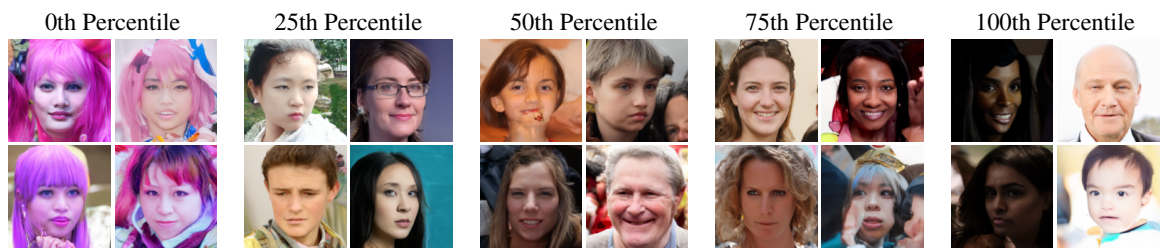


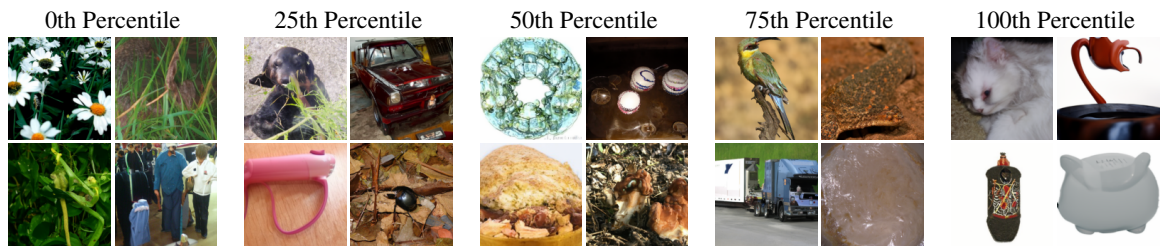
Figure 13: “Fakeness” rating of DM-generated images (LSUN Bedroom) based on predictions from detector Wang2020 fine-tuned on images from all DMs. Images are ranked by the model’s output, i.e., images in the 100th percentile are considered most fake.



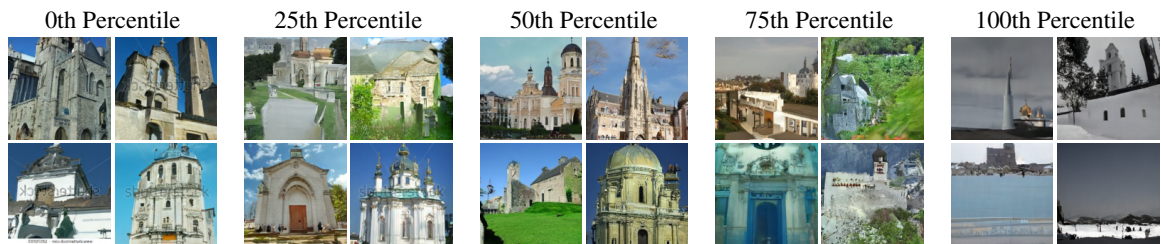
(a) LDM (FFHQ)



(b) ADM' (FFHQ)



(c) ADM (ImageNet)



(d) PNLM (LSUN Church)

Figure 14: “Fakeness” rating of DM-generated images (other datasets) based on predictions from detector Gragnaniello2021 trained on ProGAN images. Images are ranked by the model’s output, i.e., images in the 100th percentile are considered most fake.

C SUPPLEMENTAL MATERIAL ON THE FREQUENCY ANALYSIS

C.1 Descriptions of Frequency Transforms

Discrete Fourier Transform (DFT). The DFT maps a discrete signal to the frequency domain by expressing it as a sum of periodic basis functions. Given a grayscale image I with height H and width W , the two-dimensional DFT (with normalization term omitted) is defined as

$$I_{\text{DFT}}[k, l] = \sum_{x=0}^{H-1} \sum_{y=0}^{W-1} I[x, y] \exp^{-2\pi i \frac{xk}{H}} \exp^{-2\pi i \frac{yl}{W}}, \quad (4)$$

with $k = 0, \dots, H-1$ and $l = 0, \dots, W-1$. For visualization, the zero-frequency component is shifted to the center of the spectrum. Therefore, coefficients towards the edges of the spectrum correspond to higher frequencies.

Discrete Cosine Transform (DCT). The DCT is closely related to the DFT, however it uses real-valued cosine functions as basis functions. It is used in the JPEG compression standard due to its high degree of energy compaction (Wallace, 1991), which ensures that a large portion of a signal’s energy can be represented using only a few DCT coefficients. The type-II DCT, which the term DCT usually refers to, is given as

$$I_{\text{DCT}}[k, l] = \sum_{x=0}^{H-1} \sum_{y=0}^{W-1} I[x, y] \cos \left[\frac{\pi}{H} \left(x + \frac{1}{2} \right) k_x \right] \cos \left[\frac{\pi}{W} \left(y + \frac{1}{2} \right) k_y \right], \quad (5)$$

again omitting the normalization factor. In the resulting spectrum, the low frequencies are located in the upper left corner, with frequencies increasing along both spatial dimensions.

Reduced Spectrum. While the DFT provides a useful visual representation of an image’s spectrum, it is less suitable for comparing different spectra quantitatively. Therefore, previous works use the reduced spectrum, a one-dimensional representation of the Fourier spectrum (Durall et al., 2020; Dzanic et al., 2020; Schwarz et al., 2021; Chandrasegaran et al., 2021). The definition of the reduced spectrum slightly differs between different existing works, we decide to follow that of Schwarz et al. (Schwarz et al., 2021). It is obtained by azimuthally averaging over the spectrum in normalized polar coordinates $r \in [0, 1]$, $\theta \in [0, 2\pi)$ according to

$$\tilde{S}(r) = \frac{1}{2\pi} \int_0^{2\pi} S(r, \theta) d\theta \quad \text{with} \quad r = \sqrt{\frac{k^2 + l^2}{\frac{1}{4}(H^2 + W^2)}} \quad \text{and} \quad \theta = \text{atan2}(k, l), \quad (6)$$

with $S[k, l] = |I_{\text{DFT}}[k, l]|^2$ being the squared magnitudes of the Fourier coefficients. The maximum frequency is given by the Nyquist frequency $f_{\text{nyq}} = \sqrt{k^2 + l^2} = H/\sqrt{2}$ for a square image with $H = W$.

C.2 DCT Spectra

Figure 15 depicts the DCT spectra of both GANs and DMs. Similar to DFT, images generated by DMs exhibit fewer artifacts, except for LDM.

C.3 Logistic Regression Experiments

The experiments in Section 6, in particular Figures 3 and 4, demonstrate that although DMs do not exhibit strong frequency artifacts, their spectrum deviates from that of real images. A natural question is therefore whether these discrepancies can be used to detect DM-generated images more effectively. Following the work of (Frank et al., 2020), we perform a simple logistic regression on each dataset with different transforms: Pixel (no transform), DFT (and taking the absolute value), and DCT.

We use 20000 samples for training, 2000 for validation, and 20000 for testing, each set equally split between real and fake images. To reduce the number of features, we transform all images to grayscale and take a center crop with dimensions 64×64 . Additionally, all features are independently standardized to have zero mean and unit variance. We apply L_2 regularization and identify the optimal regularization weight by performing a grid search over the range $\{10^k \mid k \in \{-4, -3, \dots, 4\}\}$.

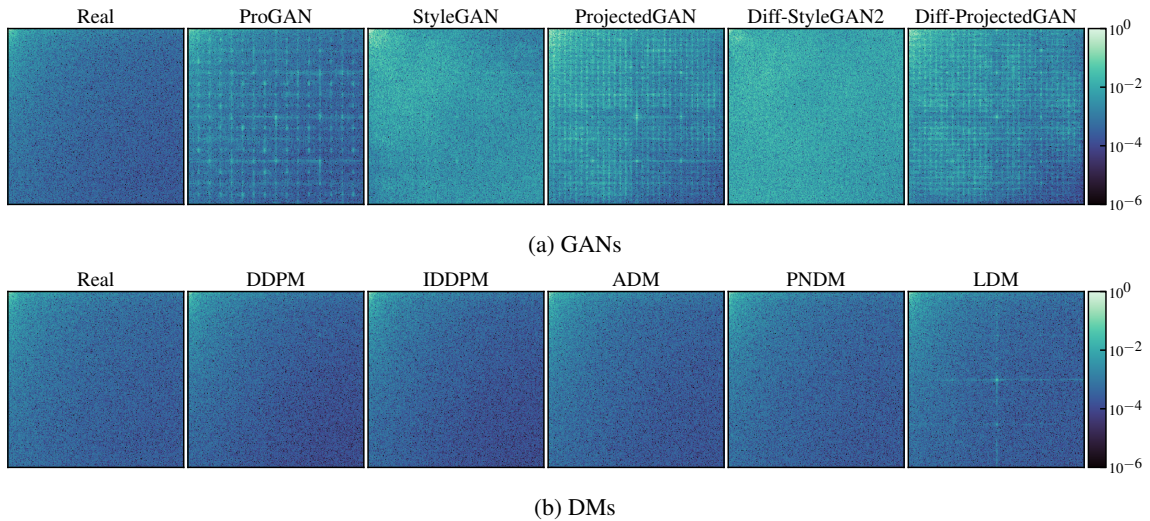


Figure 15: Mean DCT spectrum of real and generated images. To increase visibility, the color bar is limited to $[10^{-6}, 10^0]$, with values lying outside this interval being clipped.

Table 5: Accuracy of logistic regression on pixels and different transforms. Next to each transform column we report the gain compared to the accuracy on pixels.

	Pixel	DFT		log(DFT)		DCT		log(DCT)	
ProGAN	64.8	74.7	+9.9	72.6	+7.8	65.4	+0.6	74.9	+10.1
StyleGAN	91.1	87.4	-3.7	86.2	-4.9	92.6	+1.5	86.4	-4.7
ProjectedGAN	90.0	90.8	+0.8	90.3	+0.3	91.0	+1.0	95.3	+5.3
Diff-StyleGAN2	92.4	80.3	-12.0	80.5	-11.9	93.8	+1.4	87.6	-4.7
Diff-ProjectedGAN	87.4	93.9	+6.5	93.1	+5.7	88.1	+0.6	97.7	+10.3
DDPM	51.7	64.2	+12.6	64.2	+12.5	52.4	+0.7	64.3	+12.6
IDDPM	51.6	62.1	+10.6	61.7	+10.1	51.7	+0.1	61.7	+10.1
ADM	50.1	54.7	+4.6	52.3	+2.3	50.1	+0.0	53.8	+3.7
PNNDM	52.5	57.0	+4.5	58.2	+5.7	51.1	-1.4	61.4	+8.9
LDM	56.6	63.7	+7.1	66.1	+9.5	58.5	+1.9	73.0	+16.3

The accuracy of all GANs and DMs in our dataset is given in Table 5. We also report the results for log-scaled DFT and DCT coefficients, as this leads to significant improvements for some generators. For both GANs and DMs, using information from the frequency domain increases classification accuracy. On average, the performance gain of the best transform compared to no transform is 5.72 % and 10.6 %, respectively. Although the gain for DMs is more than double that for GANs, the overall maximum accuracy is significantly lower (90.9 % for GANs and 63.1 % for DMs on average). Therefore, we can not conclude that DMs exhibit stronger discriminative features in the frequency domain compared to GANs. However, these results corroborate the hypothesis that DM-generated images are more difficult to detect.

C.4 Spectrum Evolution During the Denoising Process

Analogous to Figure 5, we show the spectrum error evolution during the denoising process in Figure 16. Here, however, the error is computed relative to the spectrum of noised images at the corresponding step during the diffusion process. Similar to the denoising process, the spectra of the diffusion process are averaged over 512 samples. While the relative error is close to zero for a long time during the denoising process, the model fails to accurately reproduce higher frequencies towards $t = 0$. More precisely, too many high-frequency components are removed.

One could think that, by stopping the denoising process early, DM-generated images might be harder to detect. To test this hypothesis, we perform a logistic regression at every $0 \leq t \leq 100$ to distinguish real from increasingly denoised generated images. The model is trained using 512 real and 512 generated samples, from which 20% are used for testing. We select the optimal regularization weight by performing a 5-fold cross-

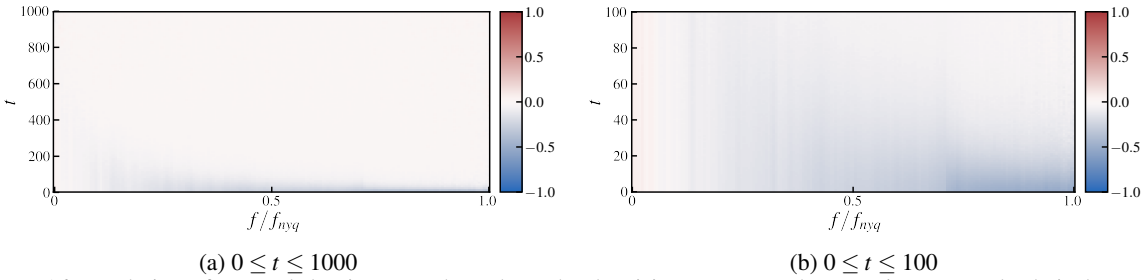


Figure 16: Evolution of spectral density error throughout the denoising process. The error is computed relatively to the corresponding step in the diffusion process. The colorbar is clipped at -1 and 1. If the model was able to perfectly denoise, the difference would be 0 at all t .

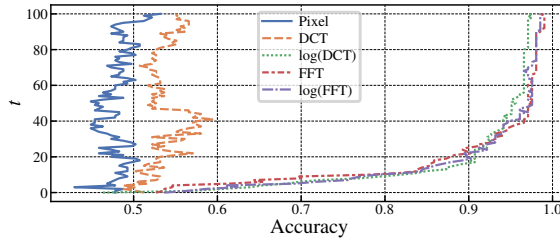


Figure 17: Accuracy of logistic regression during the denoising process. Note that only the last 100 steps of the denoising process are depicted.

validation over $\{10^k \mid k \in \{-4, -3, \dots, 4\}\}$. Similar to Section C.3, we compare the performance on pixels and different transforms. The results in Figure 17 do not indicate that around $t = 10$ fake images are less detectable. In Figure 18 it becomes apparent that at this t the images are noticeably noisier, which probably explains the increased accuracy.

C.5 Extended Analysis of Spectrum Discrepancies

Our analysis in the frequency domain (see Figure 4 in the main paper) suggests that current state-of-the-art DMs do not match the high-frequency content well. To further analyze these findings, we build on insights from the denoising autoencoder (DAE) literature. Roughly speaking, the task DAEs face is conceptually similar to the task of the noise predictor ϵ_θ in DMs at a single time step: denoising a disturbed input at a fixed noise level. Note that while we believe that DMs and DAEs can be conceptually related, the concepts are distinct in several ways: DMs use parameter sharing to perform noise prediction at multiple noise levels to set up the generation as an iterative process. On the other hand, DAEs make use of a latent space to learn suitable representations for reconstruction, classically at a fixed noise level. Nevertheless, we are convinced that it may be useful to take these insights into account.

A handy observation from DAEs relates the level of corruption to the learned feature scales: Denoising an image at small noise levels requires to accurately model fine granular details of the image, while coarse/large-scale features can still be recovered at high noise levels (see e.g., (Vincent et al., 2010; Geras and Sutton, 2015; Geras and Sutton, 2016)). Transferring this insight to DMs, we observe that the training objective guides the reconstruction performance across the different noise levels based on a weighting scheme $w(t)$ that translates to the (relative) importance of certain noise levels throughout the optimization process.

Recall that the objective of many prominent DMs can be stated as a weighted sum of mean squared error (MSE) terms

$$L(\theta) = \sum_{t=0}^T w(t) \mathbb{E}_{t, \mathbf{x}_0, \epsilon} [\|\epsilon - \epsilon_\theta(\mathbf{x}_t, t)\|^2] \quad (7)$$

usually with $T = 1000$. The theoretically derived variational lower bound L_{vlb} , which would optimize for high likelihood values, corresponds to the weighting scheme (here in the case of $\Sigma(t) = \sigma_t^2 \mathbf{I}$)

$$w(t) = \frac{\beta_t^2}{2\sigma_t^2 \alpha_t (1 - \bar{\alpha}_t)} \quad (8)$$

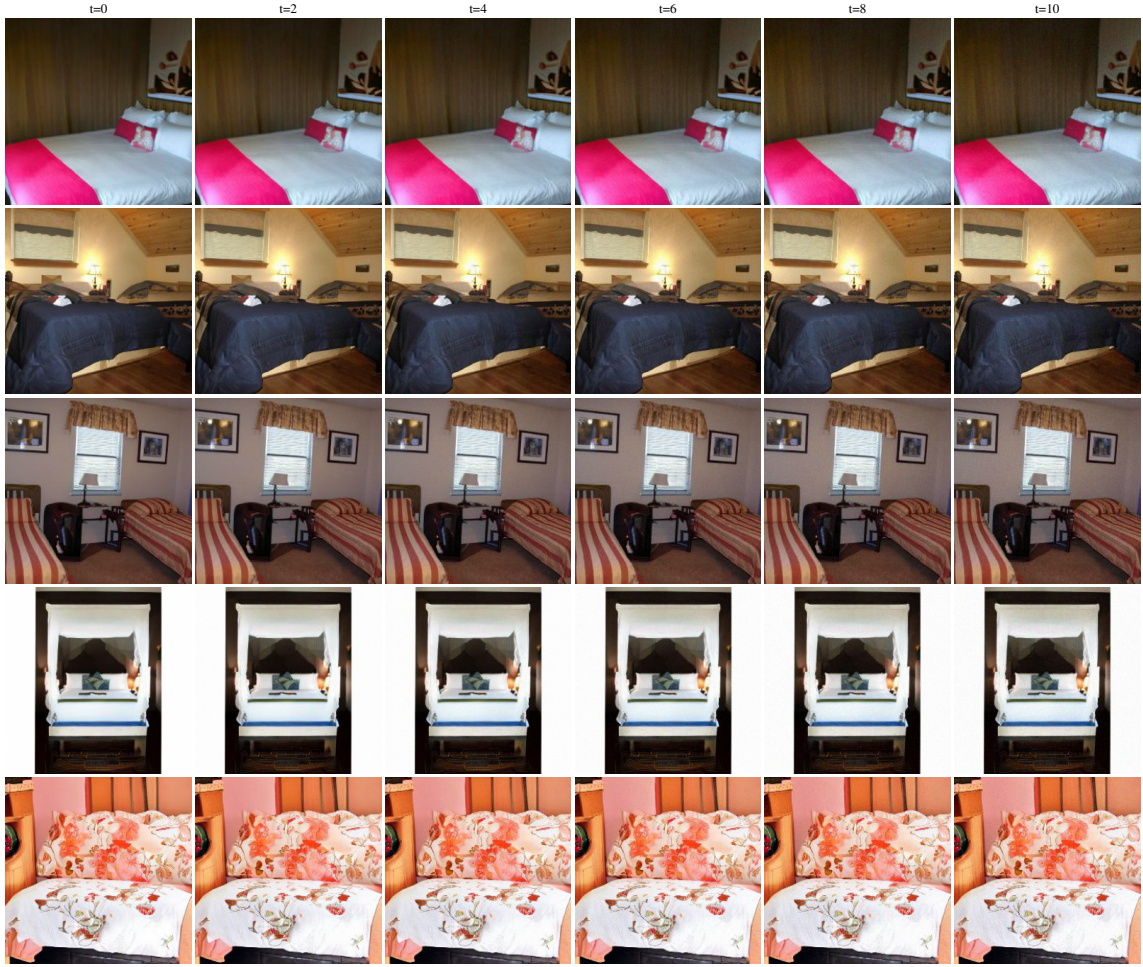


Figure 18: Example images generated by ADM at different t . When zoomed in, the high-frequency noise towards higher t becomes apparent.

with α_t and $\bar{\alpha}_t$ derived from the noise schedule β_t (see Section 3). However, L_{vib} turns out to be extremely difficult to optimize in practice (see e.g., (Dhariwal and Nichol, 2021)), arguably due to large influence of the challenging denoising steps near $t = 0$. To circumvent this issue, L_{simple} was proposed by Ho et al. (Ho et al., 2020) which corresponds to $w(t) = 1$, and turned out to be stable to optimize and already leads to remarkable perceptual quality. In order to achieve both, perceptual image quality and high likelihood values, Nichol et al. (Nichol and Dhariwal, 2021) proposed $L_{\text{hybrid}} = L_{\text{simple}} + \lambda L_{\text{vib}}$ with $\lambda = 0.001$ which increases the influence of low noise levels. The relative importance of reconstruction tasks at different noise levels for the above discussed objectives are depicted in Figure 19.

To put the above discussion in a nutshell, we hypothesize that the ability of a DM to match the real frequency spectrum is governed by the reconstruction performance at the corresponding noise levels. Importantly, successful error prediction at low noise scales, i.e., near $t = 0$, requires capturing the high-frequency content of an image (which would be the case when (successfully) optimizing L_{vib}). We deduce that the relative down-weighting of the influence of low noise levels when using L_{simple} or L_{hybrid} (compared to the theoretically derived L_{vib}) results in the observed mismatch of high frequencies.

The mean reduced spectra of various DMs (Figure 4) support this hypothesis: Both IDDPM and ADM are trained with L_{hybrid} (which incorporates a relatively higher weight on low noise levels), and are able to reduce the gap to the real spectrum when compared to the baseline (DDPM) trained with L_{simple} (Ho et al., 2020). Clearly, we believe that not only the weighting scheme $w(t)$ accounts for the resulting spectral properties, but more importantly the model’s capabilities to successfully predict the low level noise in the first place. From this perspective, the weighting scheme acts as a proxy that encourages the model to focus on specific noise levels.

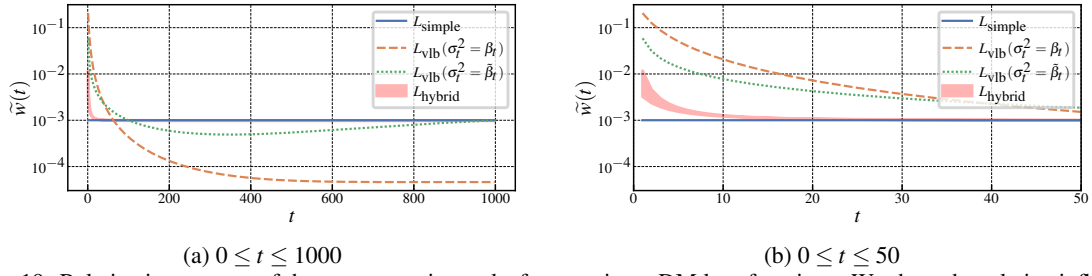


Figure 19: Relative importance of the reconstruction tasks for prominent DM loss functions. We show the relative influence $\tilde{w}(t) = w(t)/\sum_{t=0}^T w(t)$ in Equation 7 for (a) the whole denoising-diffusion process and (b) a close-up on the lowest noise levels. For L_{vlb} we depict both, lower and upper bound for the denoising variance σ_t^2 (given as $\sigma_t^2 = \beta_t$ and $\sigma_t^2 = \tilde{\beta}_t$, as defined by Ho et al. (Ho et al., 2020)). In the case of L_{hybrid} , used by IDDPM and ADM, we use $\sigma_t^2 \mathbf{I}$ for visualization purposes instead of a diagonal covariance matrix and plot $\tilde{w}(t)$ for the range of admissible variances σ_t^2 . All plots assume the linear noise schedule β_t by Ho et al. (Ho et al., 2020) and $T = 1000$.

We conclude that the objectives of DMs are well-designed to guide the model to high perceptual quality (or benchmark metrics such as FID), while falling short on providing sufficient information to accurately model the high frequency content of the target images, which would be better captured by a likelihood-based objective like L_{vlb} .

C.6 Effect of Number of Sampling Steps

Analogous to Fig. 7 we show the spectral density error using DDIM (Song et al., 2022a) in Fig. 20. As a reference, we also include the error without DDIM. Performing more steps leads to lower errors, with DDIM improving faster than normal sampling. This finding is coherent with previous results, as DDIM generates better samples at fewer sampling steps (Song et al., 2022a).

In addition, we repeat the logistic regression experiment from Appendix C.4 for samples generated with different numbers of timesteps, the results are shown in Figure 21. We also provide example images in Figure 22. As expected, images become harder to detect with more sampling steps and therefore higher image quality.

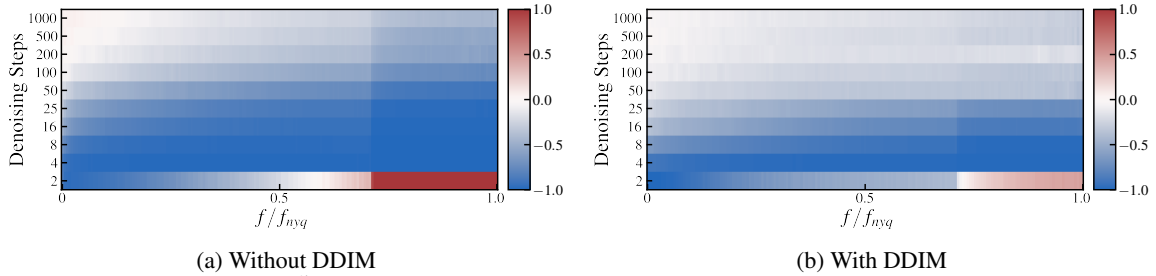


Figure 20: Spectral density error \tilde{S}_{err} for different numbers of denoising steps. The error is computed relatively to the spectrum of real images. The colorbar is clipped at -1 and 1. Note that the y-axis is not scaled linearly.

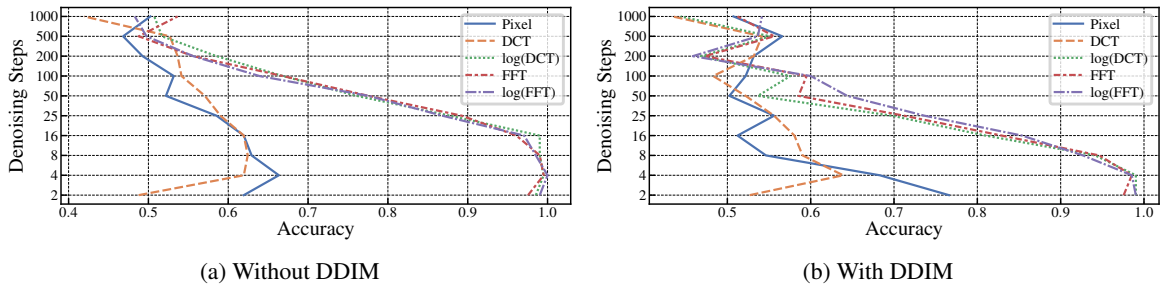
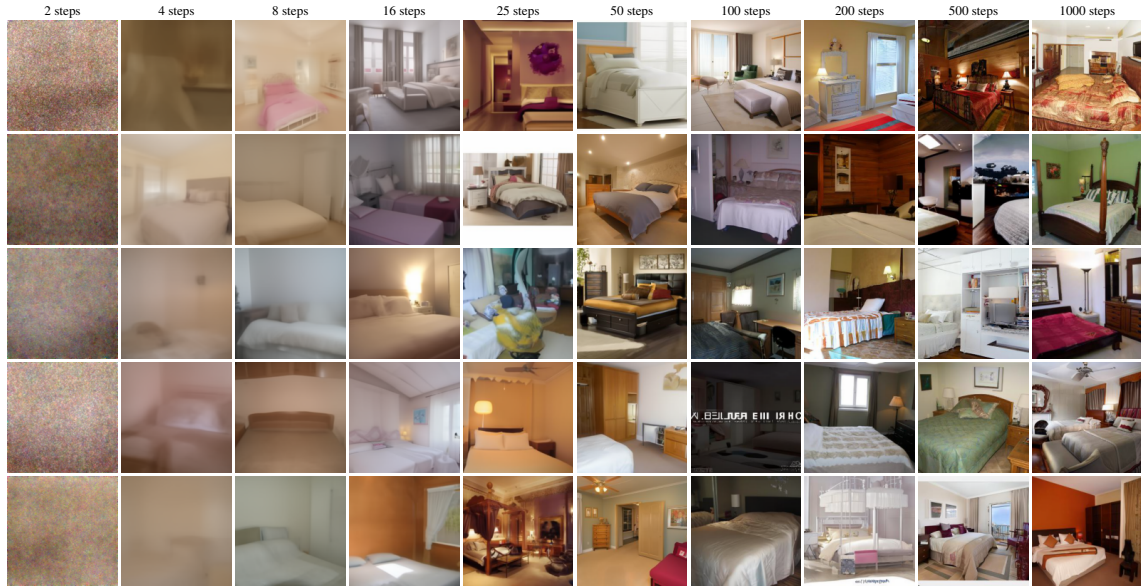
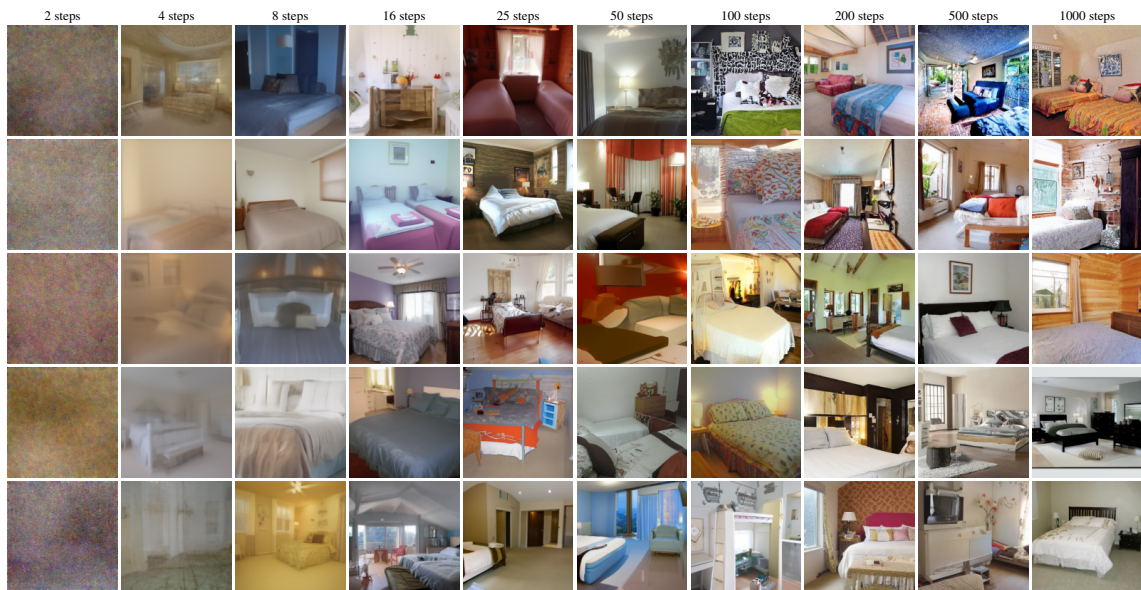


Figure 21: Accuracy of logistic regression for different numbers of sampling steps. Note that the y-axis is not scaled linearly.



(a) Without DDIM



(b) With DDIM

Figure 22: Example images generated by ADM with different numbers of sampling steps.

C.7 Frequency Analysis on Additional Datasets

We analyze the DFT (Figure 23), DCT (Figure 24), and reduced spectra (Figure 25) using a similar process as in Section 6. Regarding frequency artifacts, the results are consistent with that from LSUN Bedroom, LDM exhibits grid-like artifacts while ADM and PNDM do not. The spectra of ADM on LSUN Cat and LSUN Horse do contain irregular, vertical structures, which we did not observe for any other model and dataset. However, these are substantially different and not as pronounced as GAN artifacts. The DFT and DCT of (real and generated) FFHQ images clearly deviate from the remaining spectra, which we attribute to the homogeneity of the dataset. Note that LDM and ADM'/P2 were trained on differently processed versions of the real images, which is why we include the spectra of both variants. While we observe the known artifacts for LDM, ADM' and P2 do not contain such patterns.

The reduced spectra have largely the same characteristics as for LSUN Bedroom, except for ImageNet. Here we observe an overestimation towards higher frequencies, which is the opposite of what we see for ADM on other datasets. A possible explanation could be that the authors sampled images from LSUN using 1000 and from ImageNet using only 250 steps. We suppose that the amount of spectral discrepancies is highly training dependent.

As discussed in Section 6, the DFT and DCT spectra of images generated by Stable Diffusion exhibit very subtle grid-like artifacts. Note that we exclude images generated by Midjourney from this analysis due to the small number of available samples. The reduced spectra show similarities to those of LDM, with a rise towards the higher end of the spectrum. However, the spectral density of images generated by Stable Diffusion is higher than that of real images throughout the spectrum. It should be noted that these deviations might be caused due to the different data distributions of real and generated images.

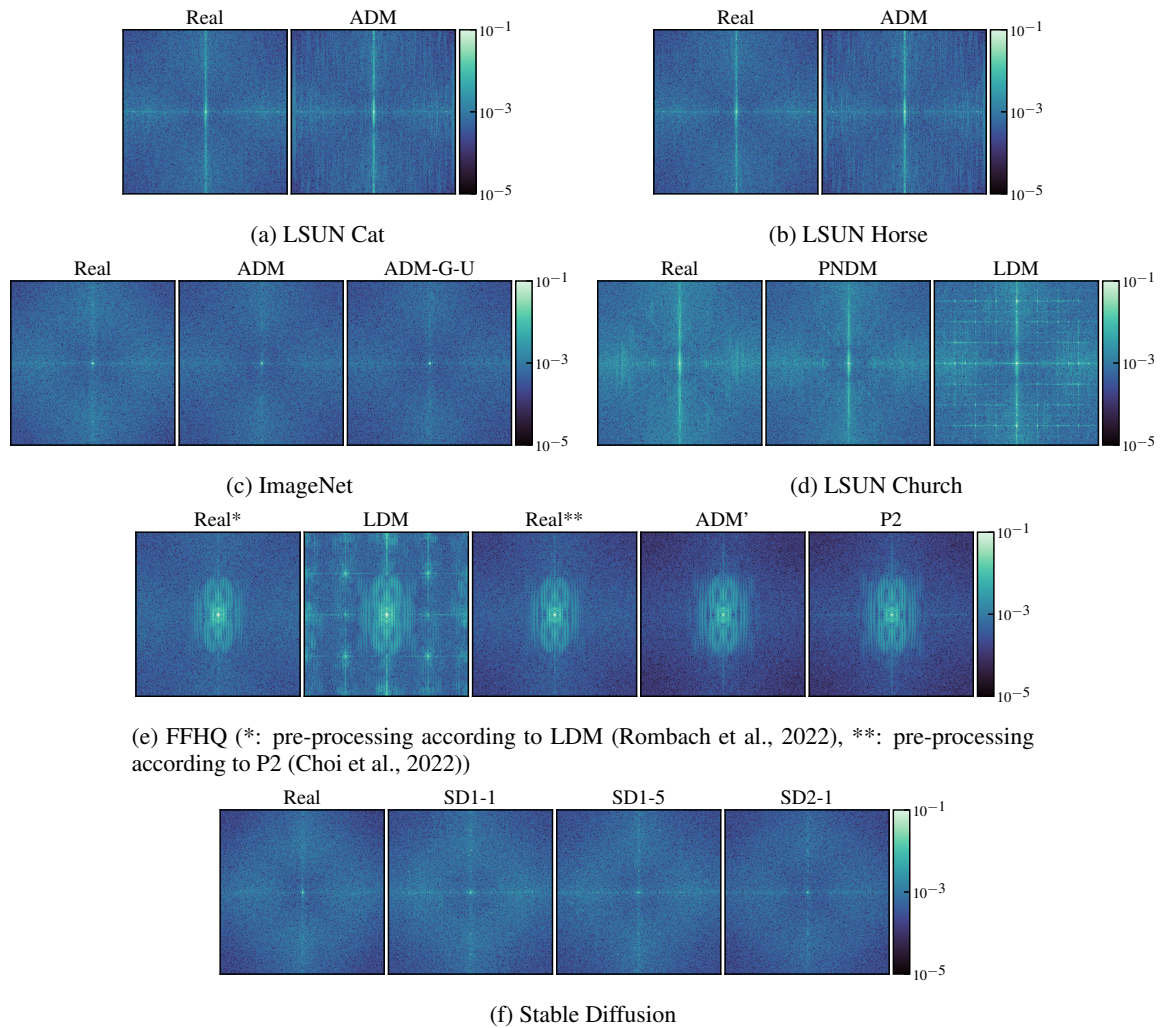


Figure 23: Mean DFT spectrum of real and generated images from additional datasets. To increase visibility, the color bar is limited to $[10^{-5}, 10^{-1}]$, with values lying outside this interval being clipped.

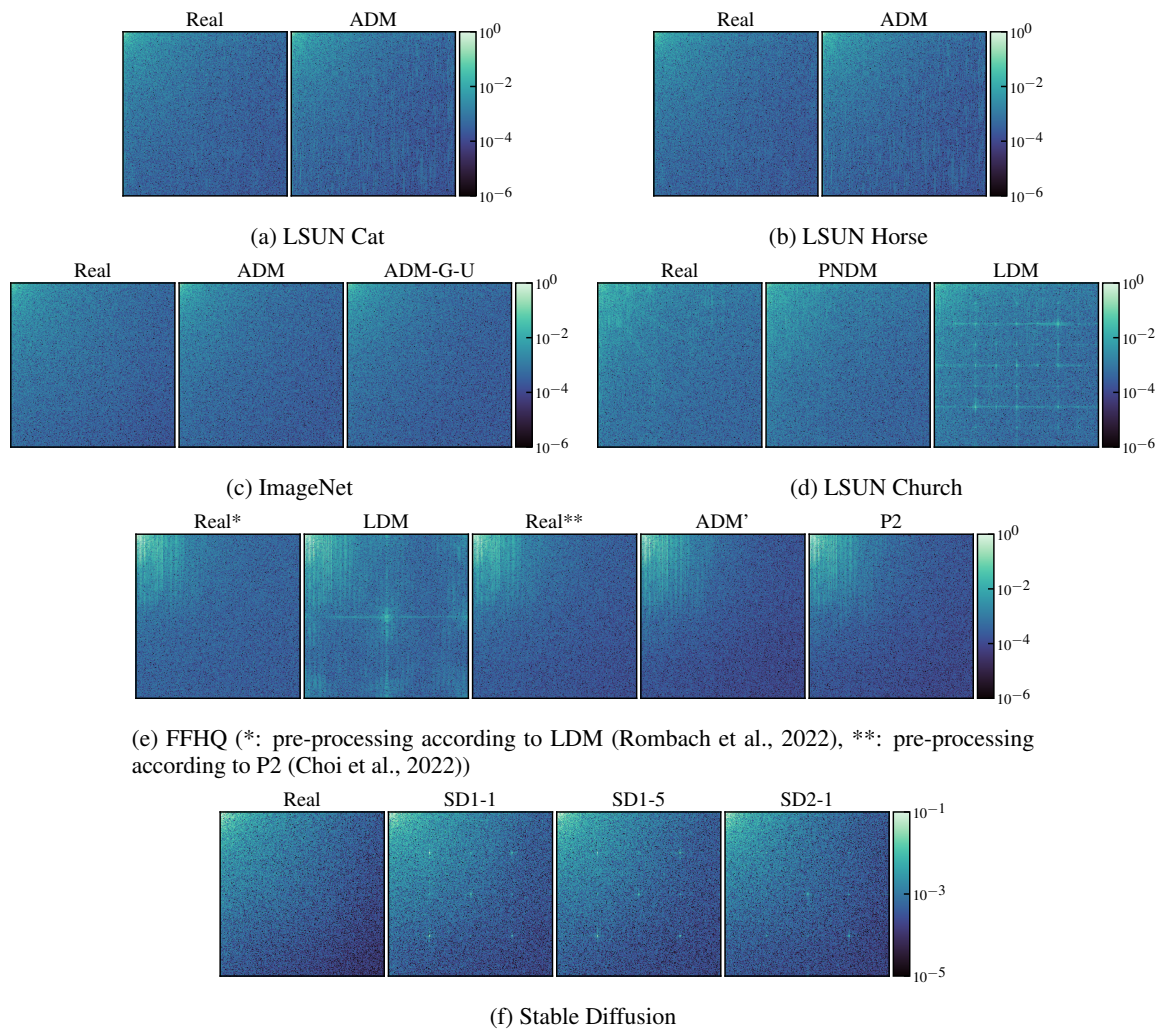
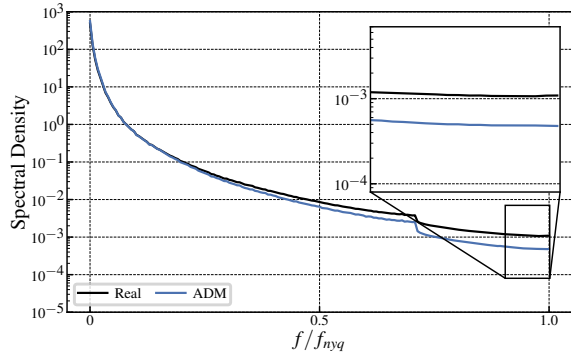
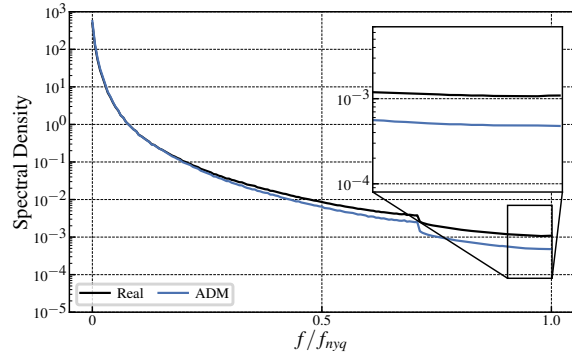


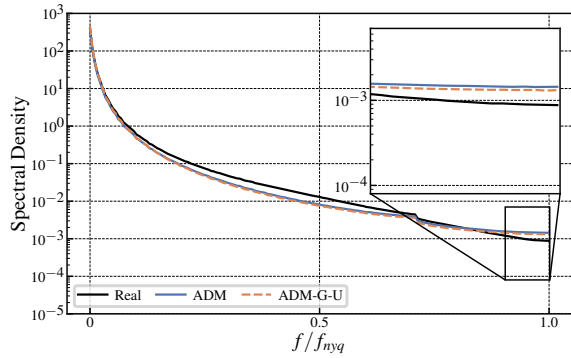
Figure 24: Mean DCT spectrum of real and generated images from additional datasets. To increase visibility, the color bar is limited to $[10^{-6}, 10^0]$, with values lying outside this interval being clipped.



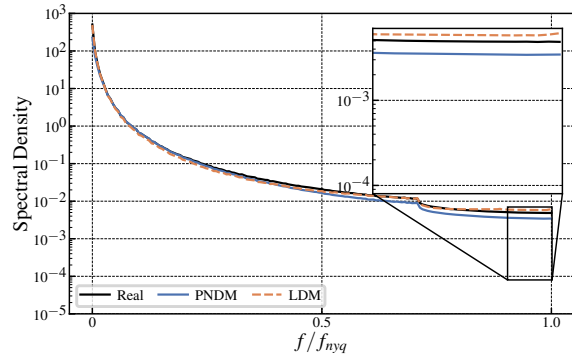
(a) LSUN Cat



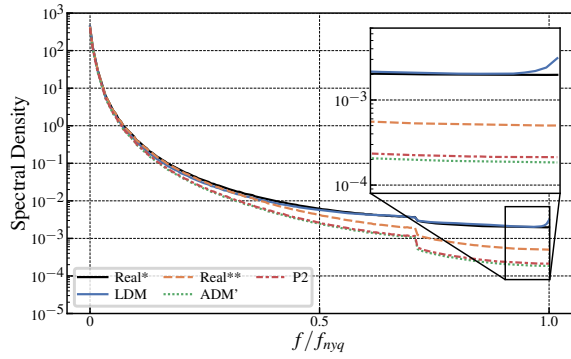
(b) LSUN Horse



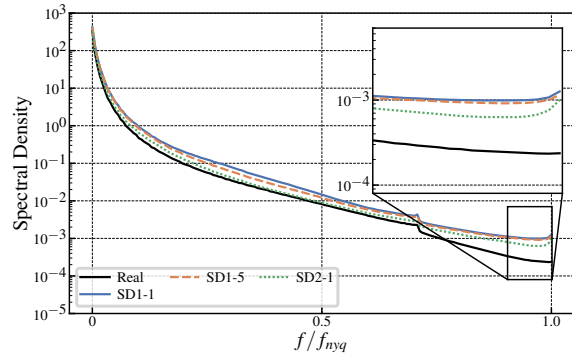
(c) ImageNet



(d) LSUN Church



(e) FFHQ (*: pre-processing according to LDM (Rombach et al., 2022), **: pre-processing according to P2(Choi et al., 2022))



(f) Stable Diffusion

Figure 25: Mean reduced spectrum of real and generated images from additional datasets. The part of the spectrum where GAN-characteristic discrepancies occur is magnified.